

X-ray emission from the Sombrero galaxy: a galactic-scale outflow

Zhiyuan Li¹, Christine Jones¹, William R. Forman¹, Ralph P. Kraft¹, Dharam V. Lal¹,
 Rosanne Di Stefano¹, Lee R. Spitler², Shikui Tang³, Q. Daniel Wang³,
 Marat Gilfanov⁴, Mikhail Revnivtsev^{5,6}

ABSTRACT

Based on new and archival *Chandra* observations of the Sombrero galaxy (M 104=NGC 4594), we study the X-ray emission from its nucleus and the extended X-ray emission in and around its massive stellar bulge. We find that the 0.3-8 keV luminosity of the nucleus appears constant at $\sim 2.4 \times 10^{40}$ ergs s⁻¹, or $\sim 10^{-7}$ of its Eddington luminosity, on three epochs between December 1999 and April 2008, but drops by a factor of two in the November 2008 observation. The 2-6 keV unresolved emission from the bulge region closely follows the K-band star light and most likely arises from unresolved stellar sources. At lower energies, however, the unresolved emission reaches a galactocentric radius of at least 23 kpc, significantly beyond the extent of the star light, clearly indicating the presence of diffuse hot gas. We isolate the emission of the gas by properly accounting for the emission from unresolved stellar sources, predominantly cataclysmic variables and coronally active binaries, whose quasi-universal X-ray emissivity was recently established. We find a gas temperature of ~ 0.6 keV with little variation across the field of view, except for a lower temperature of ~ 0.3 keV along the stellar disk. The metal abundance is not well constrained due to the limited counting statistics, but is consistent with metal-enrichment by Type Ia supernovae. We measure a total intrinsic 0.3-2 keV luminosity of $\sim 2 \times 10^{39}$ ergs s⁻¹, which corresponds to only one percent of the available energy input by Type Ia supernovae in the bulge, but is comparable to the prediction by the latest galaxy formation models for disk galaxies as massive as Sombrero. However, such numerical models do not fully account for internal feedback processes, such as nuclear feedback and stellar feedback, against accretion from the intergalactic medium. On the other hand, we find no evidence for either the nucleus or the very modest star-forming activities in the disk to be a dominant heating

¹Harvard-Smithsonian Center for Astrophysics, 60 Garden Street, Cambridge, MA 02138, USA; zyli@cfa.harvard.edu

²Centre for Astrophysics and Supercomputing, Swinburne University, Hawthorn, VIC 3122, Australia

³Department of Astronomy, University of Massachusetts, 710 North Pleasant Street, Amherst, MA 01003, USA

⁴Max-Planck-Institut für Astrophysik, Karl-Schwarzschild-Str 1, 85741 Garching bei München, Germany

⁵Excellence Cluster Universe, Technische Universität München, Boltzmannstr.2, 85748 Garching, Germany

⁶Space Research Institute, Russian Academy of Sciences, Profsoyuznaya 84/32, 117997 Moscow, Russia

source for the diffuse gas. We also show that neither the expected energy released by Type Ia supernovae nor the expected mass returned by evolved stars is recovered by observations. We argue that in Sombrero a galactic-scale subsonic outflow of hot gas continuously removes much of the “missing” energy and mass input from the bulge region. The observed density and temperature distributions of such an outflow, however, continues to pose challenges to theoretical studies.

Subject headings: galaxies: individual (M 104) – galaxies: spiral – X-rays: galaxies – X-rays: ISM

1. Introduction

Early X-ray observations of nearby galactic spheroids (i.e., elliptical galaxies and bulges of disk galaxies) have established two primary X-ray emitters: diffuse hot gas and discrete sources (e.g., Forman, Jones & Tucker 1985; Van Speybroeck et al. 1979; Trinchieri & Fabbiano 1985). The hot gas is perhaps ubiquitous in early-type galaxies, but is found to dominate the overall X-ray emission only in gas-rich, massive elliptical galaxies. In low- and intermediate-mass galaxies, the discrete sources, primarily stellar binaries whose collective emission roughly scales with the host galaxy’s stellar mass (Gilfanov 2004; Revnivtsev et al. 2007), generally overwhelm the hot gas. An X-ray nucleus, with a high incidence rate in nearby early-type galaxies (Zhang et al. 2009; Gallo et al. 2010), may further complicate the observed X-ray emission. Studies of the hot gas in the less massive early-type galaxies thus have been warranted only with the *Chandra X-ray Observatory* (Weisskopf et al. 2002), owing to its superb angular resolution for isolating discrete sources and its excellent sensitivity for tracing faint, extended X-ray emission.

Many recent efforts to study hot gas in elliptical galaxies (e.g., Fukazawa et al. 2006; Diehl & Statler 2007; Memola et al. 2009), however, have not led to a consensus on the physical properties of the hot gas and their dependence on the host properties. In particular, the amount of hot gas in these systems is found to span over two orders of magnitude for a given host stellar mass (e.g., O’Sullivan, Forbes & Ponman 2001; Ellis & O’Sullivan 2006), but the origin of this dispersion remains unclear. It is widely accepted that the hot gas originates either externally from accretion of the intergalactic medium (IGM), or internally from mass loss during normal stellar evolution. The hot gas content is thus likely dependent on galaxy age (Sansom et al. 2006), but also depends sensitively on the formation history and environment of the host galaxy (Tang et al. 2009a) as well as on-going nuclear activity (e.g., Lanz et al. 2010).

Galactic bulges are thought to resemble elliptical galaxies in their stellar populations (i.e., primarily old; e.g., MacArthur, González & Courteau 2009), but a similar assessment has not been made for their ISM. For instance, it is not clear whether bulges exhibit the same dispersion in their hot gas content as in elliptical galaxies. This lack of knowledge is due partly to the limited observational information. Indeed, while the majority of nearby ($D \lesssim 40$ Mpc) optically bright

($m_B \lesssim 12$) elliptical galaxies have been observed by *Chandra* and/or *XMM-Newton*, less than half of the optically bright early-type spiral galaxies (Sa/Sab; ~ 60 in total, Tully 1988) in the same volume have received attention by X-ray pointed observations, and just a few have deep exposures. Consequently, diffuse X-ray emission has been examined in detail in only several nearby bulges (M81, Sab, Swartz et al. 2002; NGC1291, S0/a, Irwin et al. 2002; M104, Sa, Li, Wang & Hameed, 2007, hereafter LWH07; M31, Sb, Li & Wang 2007; Bogdán & Gilfanov 2008), for which there are indications that the hot gas content is similar to that found in gas-poor elliptical galaxies (e.g., NGC4697, Sarazin et al. 2001). However, a definitive view of the properties of hot gas necessarily awaits deep X-ray observations of an extensive sample of nearby bulges.

Several facts make the Sombrero galaxy (M104=NGC4594; Table 1) an excellent target for an in-depth study of diffuse hot gas in and around a bulge: (i) It harbors a prominent stellar bulge ($M_B \approx -21.4$) as luminous as massive elliptical galaxies and thus is expected to host a substantial amount of hot gas; (ii) With a well-determined distance of 9.0 ± 0.1 Mpc, the galaxy allows for simultaneously good sensitivity and substantial coverage (out to ~ 25 kpc) that are crucial for tracing extended, low-intensity X-ray emission; (iii) The nearly edge-on (84°) view of the galaxy allows for a clean separation between its disk and bulge; (iv) As indicated by the low specific fluxes of its diffuse radio, far-infrared and $H\alpha$ emission, the galaxy shows little indication for recent star formation, minimizing the possibility of heating and/or gas ejection from the disk; (v) The galaxy is relatively isolated and thus uncertainties resulting from galaxy interactions are minimal; and (vi) The galaxy is located in a direction of relatively low Galactic foreground absorption column density ($N_{\text{HI}} = 3.7 \times 10^{20} \text{ cm}^{-2}$), essential for studying the soft X-ray emission from hot gas.

Based on shallow *Chandra* and *XMM-Newton* observations, LWH07 reported the detection of diffuse X-ray emission from Sombrero, which appears significantly more extended than the optical starlight. LWH07 took advantage of the *Chandra* angular resolution to study the inner galactic regions, where many discrete sources are present and have to be removed, and of the *XMM-Newton* field of view to trace the diffuse emission from beyond the galaxy’s optical extent. Nevertheless, the study of LWH07 was subject to several limitations: (i) The *XMM-Newton* observation, limited by its relatively large point-spread function (PSF) and high instrumental background, is far from ideal for quantifying the faint, extended X-ray emission; (ii) The instrumental heterogeneity also challenges the calibration of *Chandra* and *XMM-Newton* measurements at transition regions; (iii) Even in *Chandra* images with the bright discrete sources removed, the apparently “diffuse” X-ray emission is still contaminated by the emission from unresolved stellar objects. A common practice to account for this stellar component in the unresolved emission has been to scale the detected hard X-ray photons (e.g., with energies above 2 keV), which presumably exclusively arise from stellar objects, to predict the soft photons from the same population, by assuming an average hardness ratio the same as that of the resolved bright sources, primarily low-mass X-ray binaries (LMXBs). Not until recently has such an assumption been recognized to be problematic, following the calibration of the collective X-ray emission from fainter stellar populations, i.e., coronally active binaries and cataclysmic variables (ABs and CVs; Sazonov et al. 2006; Revnivtsev et al. 2007, 2008).

These sources exhibit a much softer collective spectrum than that of LMXBs, such that they can overwhelm faint LMXBs (i.e., those below the source detection threshold) in terms of contribution to the unresolved soft X-ray emission. An appropriate treatment is therefore needed to decompose the truly diffuse emission, fully accounting for the collective emission of ABs and CVs.

Mindful of the above concerns, we have recently obtained two new *Chandra* observations of the Sombrero galaxy to advance our view of high-energy stellar and interstellar phenomena in a galactic bulge. Based on the new data, Li et al. (2010, hereafter Paper I) studied LMXBs in Sombrero. The present work focuses on the X-ray emission from the diffuse hot gas and from the nucleus. § 2 describes the data preparation toward extracting the extended, unresolved X-ray emission. § 3 presents the step-by-step analysis of the nuclear emission and the extended emission on various scales, with an emphasis on the procedure of isolating the truly diffuse emission from the hot gas. § 4 discusses the origin and fate of the hot gas, particularly in the scope of a galactic-scale outflow. The study is summarized in § 5. Quoted errors are at the 90% confidence level throughout this work unless otherwise noted.

2. Data preparation

Chandra observed Sombrero on four occasions over a decade. The first observation (ObsID 407; PI: G. Garmire) was taken on December 20, 1999, in a 1/8 sub-array mode with a short exposure of 1.8 ks. The data helped demonstrate the presence of a bright X-ray source coincident with the galactic nucleus (Ho et al. 2001; Pellegrini et al. 2002). The second observation was taken on May 31, 2001 (ObsID 1586; PI: S. Murray), with a 19-ks exposure in the ACIS-S FAINT mode, which was used to study the X-ray source population (e.g., Di Stefano et al. 2003) and the hot gas (LWH07). On April 29 and December 2, 2008 we obtained two new observations (ObsID 9532 and 9533; PI: C. Jones), in the ACIS-I VFAINT mode with exposures of 85 and 90 ks, respectively. In Paper I, data of ObsID 1586, 9532 and 9533 are used to study the discrete X-ray sources. In this work we utilize these three observations to study the diffuse emission, chiefly based on data from the ACIS-I CCDs of ObsID 9532 and 9533 and from the S3 CCD of ObsID 1586. We also use data from the S2 CCD of ObsID 9532 and 9533 to better constrain the local sky background in our spectral analysis. In addition, to study the nucleus, we include data from ObsID 407, taking advantage of its shorter readout frame time (0.4 second, compared to the standard 3.2 second).

We reprocessed the data using CIAO v.4.1 and the corresponding calibration files, following the *Chandra* ACIS data analysis guide. Examination of the light curves indicates that the instrumental background of each observation was fairly quiescent. Subsequently, background filtering is only necessary for ObsID 1586, which results in 16.7 ks of good time intervals for this data set. For each observation, we produced count and exposure maps in the 0.4-0.7, 0.7-1, 1-2 and 2-6 keV bands, using a spatial binning factor of 2 ($\sim 1''$ per image pixel). An absorbed power-law spectrum, with a photon index of 1.7 and an absorption column density $N_{\text{H}} = 10^{21} \text{ cm}^{-2}$, was adopted as a weighting function when producing the exposure maps. The energy-dependent difference of effective

area between the ACIS-S3 CCD and the ACIS-I CCDs was also accounted for, so that the quoted count rates throughout this work are referred to ACIS-I. Corresponding instrumental background maps were generated from the “stowed” data, after calibrating with the 10-12 keV count rate. These individual maps were then projected to a common tangential point, here the optical center of Sombrero, to produce summed images of the combined field of view (FoV; cf. Fig. 1 of Paper I). The total effective exposure, in the 2-6 keV band for instance, is $\gtrsim 180$ ks within a projected galactocentric radius $R \approx 4'$, where the FoV is common to the three observations (ObsID 1586, 9532 and 9533), and gradually drops below 80 ks at $R \gtrsim 8'$.

We detected 383 discrete sources across the combined FoV, the bulk of which are LMXBs associated with Sombrero, as well as background AGNs (Paper I). To isolate the unresolved X-ray emission, we have excluded these sources from maps in individual observations, each with a circle enclosing $\sim 96\%$ of the source photons. Such a source subtraction procedure works well except for the bright nucleus, whose PSF-scattered photons contribute substantially to the unresolved emission, especially at energies above 2 keV, within the central half-arcminute. We therefore relied on *MARX* simulations (see § 3.1) to determine the expected distributions of PSF-scattered photons from the nucleus. Residual PSF-scattered photons from other sources are estimated to contribute $\sim 25\%$ of the remaining unresolved X-ray emission in the 2-6 keV band.

Due to the variation of the local background, PSF and effective exposure across the FoV, the limiting flux for source detection necessarily varies with sky position, roughly increasing with angular distance from the galactic center. Consequently, at larger radii the background contains more photons from unresolved sources. We statistically corrected for such a non-uniform background, based on the luminosity functions of the LMXBs and cosmic AGNs (Paper I), to a common source flux limit of 10^{-15} ergs s $^{-1}$ cm $^{-2}$ (0.4-6 keV) across the FoV.

We also accounted for artifacts due to photons registered during CCD readout, following the technique proposed by Markevitch et al. (2000). The procedure effectively generated maps of statistically-sampled readout photons for individual observations, which can then be projected in the same way as for the count maps.

The three terms considered above, namely, the PSF wing of the nucleus, the spatially non-uniform photons from unresolved sources, and the out-of-time events, all contribute to the unresolved emission depending on the energy band and sky position. We added these three terms to the instrumental background to form a fiducial background to be subtracted. A presumably uniform sky background, e.g., from Galactic foreground emission, is then determined locally (see § 3.4).

3. Analysis and results

3.1. The X-ray nucleus

Sombrero hosts a super-massive black hole (SMBH) with a mass of $\sim 10^9 M_{\odot}$ (Kormendy 1988; Kormendy et al. 1996) inferred from its central stellar kinematics. Classified as a LINER (low-ionization nuclear emission region; Heckman 1980; Ho, Filippenko, Sargent 1997), Sombrero is known to exhibit a low level of nuclear activity. In particular, the nucleus (i.e., the SMBH) manifests itself as a moderately bright X-ray source (Fabbiano & Juda 1997; Ho et al. 2001), as clearly seen in Fig. 1, a stacked image (i.e., combining the four *Chandra* observations) of the 0.3-8 keV emission from the central $10''$ by $10''$ region of Sombrero. The upper panel of Fig. 2 further shows the same region as detected in the individual observations. These images are shown on a refined pixel scale (1/4 of the original ACIS pixel) to take advantage of the sub-pixel positioning information that results from telescope dithering. The sub-arcsec resolution afforded by *Chandra* is ideal for disentangling the nucleus. Nevertheless, quantification of the nuclear emission demands caution on the effects of photon pile-up and PSF scattering.

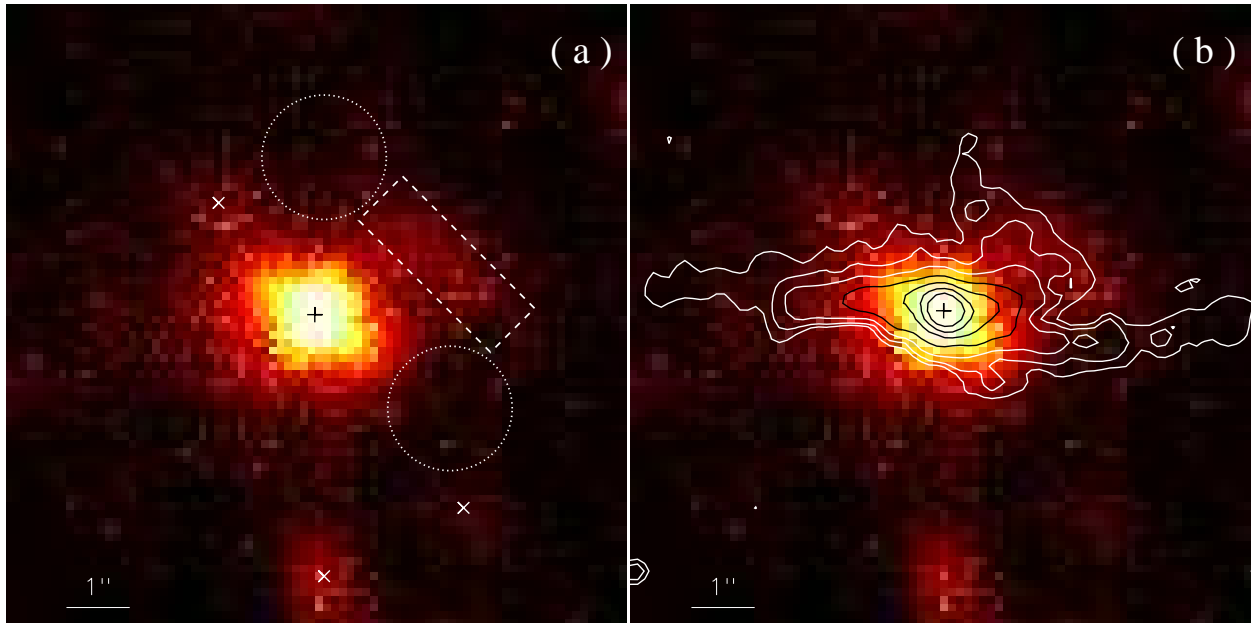


Fig. 1.— A 0.3-8 keV count image from the nucleus and its $10'' \times 10''$ (~ 430 pc by 430 pc) vicinity, on a pixel scale of one fourth of the ACIS pixel size $0''.492$. In (a), the $3'' \times 1''$ dashed rectangle outlines the region where the spectra of an apparently extended X-ray feature are extracted, while the two dotted circles show the adopted background region. The centroid of the nucleus is marked by a plus sign, while crosses highlight three point-like X-ray sources. In (b), intensity contours of the $H\alpha + [N \text{ II}]$ emission obtained from *HST* observations are plotted. Note the positional coincidence between the extended X-ray feature and the optical line emission northwest of the nucleus.

The moderately bright nucleus (with a flux of $\sim 10^{-12}$ ergs s $^{-1}$) is expected to cause mild pile-up. Direct evidence of pile-up comes from examination of events flagged as grade 7 in the raw (i.e., level 1) event file (the reprocessed, i.e., level 2, data keeps only “good” events with grades 0, 2, 3, 4, 6). When pile-up occurs, i.e., two or more photons land on the same CCD frame and consequently only one event is registered, a grade-7 event can be produced due to, for instance, a combination of grades 2-2 or grades 3-4. Visual inspection reveals that grade-7 events are clustered in the central 3 pixels around the nucleus in ObsID 1586, 9532 and 9533, but are essentially absent in ObsID 407, presumably due to the much shorter frame time of the latter.

We examine the PSF by using simulations provided by the CIAO tools *ChaRT*¹ and *MARX*². By taking the incident source spectrum (based on a *posteriori* knowledge from the spectral analysis; see below), the source location on the detector and the desired exposure, *ChaRT* traces simulated rays that can be processed by *MARX* to generate simulated events, as if registered in a real observation. The effect of pile-up can also be mimicked by *MARX*, based on the algorithm of Davis (2001). 0.3-8 keV events from the nucleus are thus simulated for the four individual observations and are shown in the lower panel of Fig. 2. General agreement between the observed and simulated images is readily seen, especially in ObsID 9532 and 9533 where the nucleus is located at a relatively large off-axis angle ($\sim 2'$) and hence the PSF elongation along a northeast-southwest direction is significant. More quantitatively, we compare the observed and simulated radial intensity profiles, shown in Fig. 3a, which are constructed by combining the 0.3-8 keV counts registered in individual observations for each of the four quadrants. The second (northeast; 90° - 180°) and fourth (southwest; 270° - 360°) quadrants show higher intensities, again due to the PSF elongation. The simulated profiles follow the observed profiles in all four quadrants in the central two pixels ($\sim 1''$) where $\sim 80\%$ of the nuclear flux is enclosed; deviations become substantial at larger off-center distances presumably due to the presence of extra-nuclear emission (e.g., arising from discrete sources and diffuse hot gas; see § 3.2) that is not simulated. The goodness of the simulated PSF is further supported in Fig. 3b, where it is compared with the intensity profile obtained by stacking several discrete sources located within $\sim 20''$ of the nucleus. The stacked intensity profile is expected to represent the actual PSF at the position of the nucleus, averaged among the four observations. Taking into account the local background, the stacked and simulated profiles agree well with each other, except in the central pixel, presumably due to the fact that the discrete sources are individually free of photon pile-up, while the much brighter nucleus is mildly so.

Next we quantify the spectral property of the nucleus. Spectra are extracted from a 2-pixel ($1''$) radius circle around the nucleus for individual observations. Fig. 3 indicates that the local background can be neglected for this relatively small aperture. An absorbed power-law (PL), modified by the pile-up model of Davis (2001), is used to fit the spectra. The spectra were first fitted individually. We found that an acceptable fit was obtained for each spectrum and the

¹<http://cxc.harvard.edu/chart/>

²<http://space.mit.edu/CXC/MARX/>

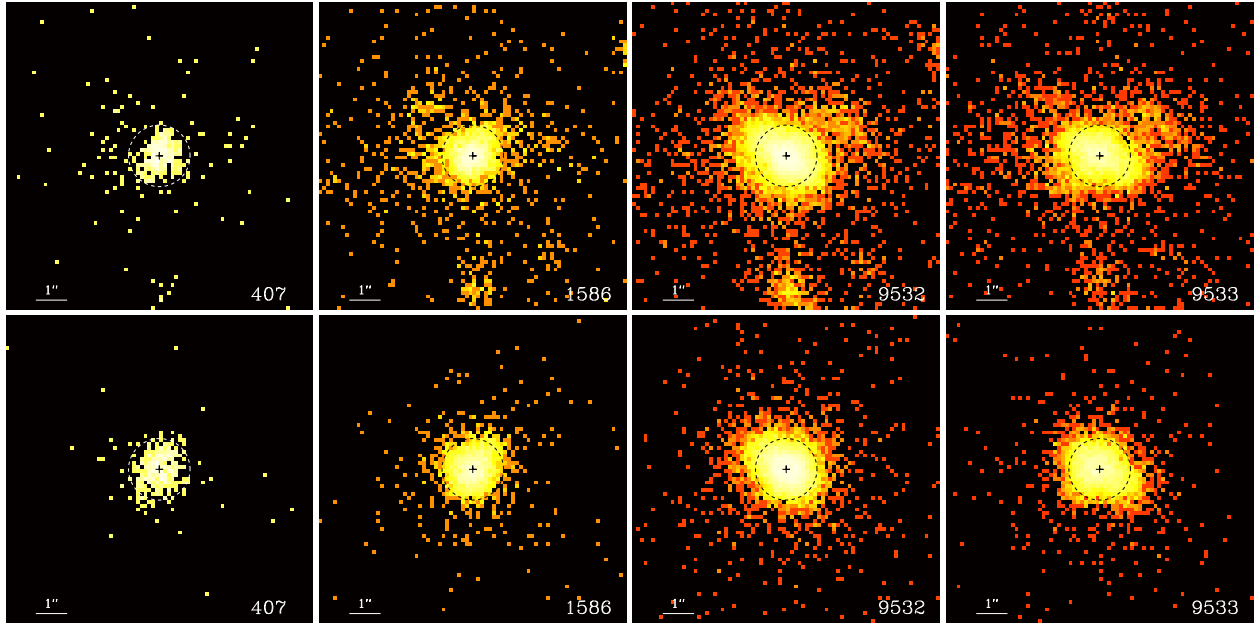


Fig. 2.— *Upper panel*: 0.3-8 keV X-ray emission from the nucleus and its $10'' \times 10''$ (~ 430 pc by 430 pc) vicinity, detected in four *Chandra* observations, on a pixel scale of one fourth of the ACIS pixel size $0''.492$. The dashed circle outlines the region where the spectra of the nucleus are extracted. *Lower panel*: Simulated 0.3-8 keV X-ray emission from the nucleus for the four observations, using the CIAO tool *ChaRT*. The centroid of the nucleus is marked by a plus sign.

resultant photon indice (Γ) and absorption column densities (N_{H}) are consistent with each other within statistical uncertainties. We note that the inclusion of the pile-up model leads to a steeper PL (i.e., a larger photon index) for the spectra of ObsID 1586, 9532 and 9533, but not for the spectrum of ObsID 407. This supports the above argument that the nucleus is not subject to pile-up in ObsID 407. We then fit the spectra simultaneously, forcing both Γ and N_{H} to be identical in order to reduce the statistical uncertainty. The fit was acceptable with a $\chi^2/\text{dof} = 526.7/474$, giving $\Gamma = 1.98^{+0.08}_{-0.12}$ and $N_{\text{H}} = 3.4^{+0.1}_{-0.2} \times 10^{21} \text{ cm}^{-2}$. Consistent fit results on these two parameters have been reported, based on, e.g., the *XMM-Newton* (Pellegrini et al. 2003), *BeppoSAX* (Pellegrini et al. 2002) and *ASCA* (Nicholson et al. 1998) spectra that are of much poorer angular resolutions and necessarily contaminated by extra-nuclear emission that requires additional spectral components.

In the fit the normalization was allowed to vary among the four spectra, resulting in $3.9^{+0.4}_{-0.4}$, $3.7^{+0.3}_{-0.3}$, $3.8^{+0.1}_{-0.1}$ and $1.9^{+0.1}_{-0.2} \times 10^{-4}$ for ObsID 407, 1586, 9532 and 9533, respectively. Therefore during the last observation, ObsID 9533, the nucleus shows a factor of two lower flux than in the first three observations. Corrected for absorption and the enclosed energy fraction within the spectral extraction region, which varies between 76%-83% according to the simulated PSFs for the four observations, the 0.3-8 keV intrinsic nuclear flux is $\sim 2.5, 2.4, 2.6$ and $1.3 \times 10^{-12} \text{ ergs s}^{-1} \text{ cm}^{-2}$ in ObsID 407, 1586, 9532 and 9533, respectively. This means that the X-ray luminosity of the

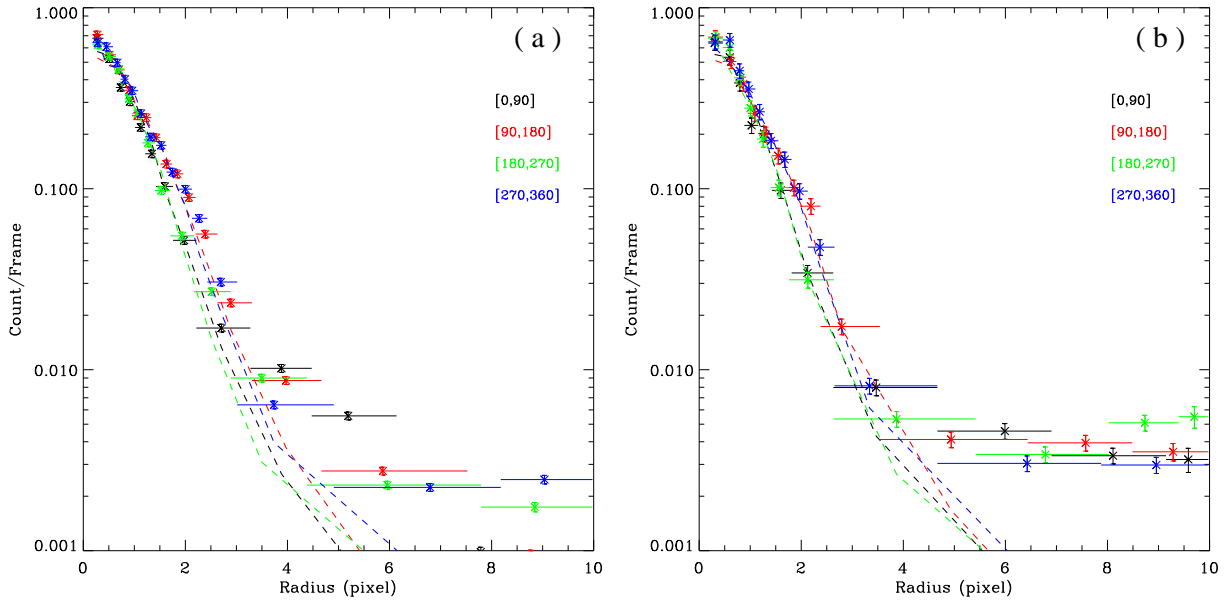


Fig. 3.— (a) 0.3-8 keV radial intensity profiles around the nucleus (color-coded data points, adaptively binned to achieve a minimum of 400 counts per bin), extracted from the combined image of the four observations, for four quadrants whose angular ranges (measured counterclockwise from west) are color-coded as shown. The curves are the corresponding profiles extracted from the *ChaRT*-simulated image. The vertical axis is in units of count/frame, where one frame is defined as 3 pixel \times 3 pixel \times 3.2 s. (b) Similar to (a), but the data points, adaptively binned to achieve a minimum of 100 counts per bin, are from stacking a few bright discrete sources located in the vicinity of the nucleus and then multiplied by a factor of 5 to match the intensity profile of the nucleus. Vertical error bars are of 1σ .

nucleus might have been constant at $\sim 2.4 \times 10^{40}$ ergs s $^{-1}$ between December 1999 and April 2008, but then dropped by a factor of two in 7 months. We also searched for, but found no evidence of, intra-observation variability of the nucleus in any individual observation.

We note that adding a Gaussian line at 6.4 keV or 6.7 keV (i.e., from iron $K\alpha$) does not statistically improve the best-fit absorbed PL model. We constrain the equivalent width (EW) of a possible Fe $K\alpha$ line by setting the normalization of the Gaussian such that the χ^2 is increased by a value of 9. For a 6.4 keV line, we obtain a 3σ upper limit on the EW of 110 eV for a narrow line (assuming $\sigma_E=0$) and of 190 eV for a broad line (assuming $\sigma_E=0.5$ keV). For a 6.7 keV line, the corresponding values are 240 eV (narrow line) and 280 eV (broad line).

3.2. The circumnuclear X-ray emission

Several features are clearly present in the circumnuclear region, including three discrete sources (each marked by a cross in Fig. 1a) and an apparently extended feature northwest of the nucleus (approximately enclosed by a dashed rectangle in Fig. 1a). We extract spectra for the extended feature from all observations except ObsID 407, from which we can only estimate 4.7 ± 3.2 (1σ) net counts, or a net count rate of $(2.6 \pm 1.8) \times 10^{-3}$ cts s $^{-1}$ for the feature. We note that the adopted background region (defined by two dotted circles in Fig. 1) encloses approximately the same amount of the PSF-scattered nuclear flux per unit area as in the rectangle. The spectra were first fit individually with an absorbed PL model. The resultant parameters are statistically consistent among the three spectra. Hence we fit the spectra simultaneously, linking all parameters. The fit is acceptable with a $\chi^2/\text{dof} = 33.4/30$, giving $\Gamma = 1.64_{-0.18}^{+0.26}$, $N_{\text{H}} = 1.4_{-0.7}^{+1.4} \times 10^{21}$ cm $^{-2}$, and a 0.3-8 keV intrinsic luminosity of 3.6×10^{38} ergs s $^{-1}$. This model predicts a net count rate of 6.2×10^{-3} cts s $^{-1}$ to be measured in ObsID 407, i.e., $\sim 2\sigma$ higher than the observed value.

The extended X-ray feature is particularly interesting in view of its possible relation with the nucleus. Gallimore et al. (2006) found in Sombrero a kpc-scale linear radio structure, which they suggested originates from a SMBH-powered jet/outflow. The position of the X-ray feature relative to the nucleus is coincident with that of the radio structure, i.e., at a position angle $\sim 45^\circ$ west of north. We investigated the Very Long Array archival data on arcsec-scales but found no evidence for extended radio emission coincident with the X-ray feature. Alternatively, the X-ray feature may originate from scattered nuclear emission and/or a photoionized gas, which requires the presence of circumnuclear dusty gas at the location of the X-ray feature. *HST* observations have resolved the narrow line region (NLR) in H α + [N II] emission, which mainly consists of a core and two arms lying east-west, i.e., in the edge-on disk (Emsellem & Ferruit 2000; Masegosa et al. 2010; Fig. 1b). Another curved H α + [N II] feature is evident northwest of the nucleus, and interestingly, is roughly coincident with the extended X-ray feature (Fig. 1b). The two arms, but not the curved feature, are also clearly seen as dust extinction against the starlight (Emsellem & Ferruit 2000). If both the H α + [N II] and X-ray emission arise from a photoionized gas, the extended feature is likely associated with the hypothesized jet/outflow and is thus located out of the disk. However, this is not readily evident in the NLR kinematics (Emsellem & Ferruit 2000). For reference, we estimate an H α + [N II] luminosity of $\sim 5 \times 10^{38}$ erg s $^{-1}$ for the feature, which is comparable to the X-ray luminosity from the same region. When associated X-ray emission is detected, NLRs often exhibit comparable luminosities in their X-ray and optical line emission (e.g., Bianchi, Guainazzi & Chiaberge 2006). Nevertheless, we note that the spectra of the X-ray feature show no sign of emission lines that are expected to arise from a photoionized gas. On the other hand, if powered by star formation, the H α + [N II] luminosity indicates a star formation rate of only $\sim 10^{-4}$ M $_{\odot}$ yr $^{-1}$ (e.g, Kennicutt 1998), which is too low to produce the observed X-ray emission from the feature. Lastly, the X-ray feature may be overlapping stellar sources. This is consistent with the fitted photon index of ~ 1.6 , typical of LMXBs, but requires at least two LMXBs of near-Eddington luminosity (for an accreting neutron star) coincidentally aligned. The lower count rate measured

in ObsID 407 would further imply flux variability for both sources. Future radio/optical/X-ray observations may help distinguish the above scenarios for this interesting feature.

To characterize the properties of the circumnuclear hot gas, we further extracted spectra from a 3''-5'' annulus around the nucleus, from ObsID 1586, 9532 and 9533, in which discrete sources and the extended feature are excluded. For simplicity, we use the FTOOL *addspect* to coadd the spectra. The coadded spectrum is fit by an absorbed MEKAL+PL model. The PL component, with a fixed photon index of 1.9, is applied to represent the contributions from the PSF-scattered nuclear flux and the residual flux of stellar sources. The MEKAL component, with the abundance fixed at solar, constrains the diffuse hot gas. The fit is acceptable with $\chi^2/\text{dof} = 24.6/19$, giving a gas temperature of $0.52^{+0.12}_{-0.22}$ keV and a gas density of $0.13^{+0.04}_{-0.02}$ cm⁻³, assuming that the diffuse emission comes from gas filling a spherical shell. Our results are consistent with the finding of Pellegrini et al. (2003) based on the data of ObsID 1586. The gas has a cooling timescale of $\sim 5 \times 10^7$ yr, according to the cooling function of Sutherland & Dopita (1993).

Assuming that the nucleus is powered by Bondi (1952) accretion of the circumnuclear hot gas, the accretion rate can be estimated as

$$\begin{aligned} \dot{M}_{\text{Bondi}} &\approx 4\pi\lambda\mu m_{\text{H}}n(GM_{\text{BH}})^2c_s^{-3} \\ &\approx 1.8 \times 10^{-3} \left(\frac{n}{0.1 \text{ cm}^{-3}}\right) \left(\frac{M_{\text{BH}}}{10^9 M_{\odot}}\right)^2 \left(\frac{kT}{0.5 \text{ keV}}\right)^{-1.5} M_{\odot} \text{ yr}^{-1}, \end{aligned} \quad (1)$$

where λ is a numerical factor taken to be 0.25, $c_s = (\gamma kT/\mu m_{\text{H}})^{1/2}$ is the sound speed, and the remaining symbols have conventional meanings. The corresponding *Bondi luminosity* is $L_{\text{Bondi}} \equiv \eta \dot{M}_{\text{Bondi}} c^2 \approx 1.0 \times 10^{43} (\eta/0.1)$ ergs s⁻¹, where η is the radiation efficiency. It follows that $L_{\text{X}}/L_{\text{Bondi}} \sim 10^{-3}$, or $L_{\text{X}}/L_{\text{Eddington}} \sim 10^{-7}$, indicating that the nucleus is radiatively inefficient, as first noted by Pellegrini et al. (2003). We also note that the *Bondi radius*, $R_B \equiv 2GM_{\text{BH}}/c_s^2 \approx 105$ pc, spans an angle of 2''.4. However, the PSF wing of the bright nucleus hampers the possibility of resolving the accretion flow.

3.3. The galactic-scale X-ray emission

3.3.1. Broad band distributions

At the galactic scale, the unresolved (i.e., source- and background-subtracted) X-ray emission in the four bands is shown in Fig. 4, in comparison with a 2MASS K-band image (Jarrett et al. 2003) that traces the old stellar populations in Sombrero. The 2-6 keV (hereafter hard band) emission traces the starlight (Fig. 4c), indicating a stellar origin. Indeed, the contribution of diffuse gas with a typical sub-keV temperature is expected to be negligible at energies above 2 keV. The hard band emission shows some asymmetry toward the northwest (outlined by a circle in Fig. 4d), although we stress caution when examining a smoothed image. We suggest that this asymmetry is due to residual particle contamination or a background object.

At energies below 2 keV, the X-ray emission appears significantly more extended than that of the K-band starlight (Fig. 4a-b). This indicates that diffuse hot gas is present in and around the bulge of Sombrero. More quantitatively, we compare the radial distributions of the X-ray emission and the K-band light. As shown in Fig. 5, the hard band radial distribution closely follows that of the K-band light within $R \approx 2'$. Indeed, a normalized K-band profile is found to be an adequate characterization of the hard band distribution (green curve in Fig. 5; the excess point at $\sim 2'.5$ is due to the anomalous feature mentioned above). The normalization factor in this case is $(7.0 \pm 1.2) \times 10^{-5}$ cts s $^{-1}$ /(MJy sr $^{-1}$). This supports the expectation that the hard band emission arises from old stellar populations, namely, unresolved LMXBs, CVs and ABs (§ 1). In particular, the CV+AB populations appear to show a quasi-universal X-ray emissivity (per unit stellar mass) in the hard band, which has been calibrated to $\sim 30\%$ uncertainty (Revnivtsev et al. 2007). In Sombrero, such a component is expected to account for $(3.4 \pm 1.0) \times 10^{-5}$ cts s $^{-1}$ /(MJy sr $^{-1}$) in the hard band. The rest, about half, of the hard band emission can be attributed to unresolved LMXBs and the PSF residuals of resolved LMXBs.

The stellar contribution to the soft bands can be determined by scaling the hard band emissivity, with certain assumptions on the integrated spectral shape of the individual stellar populations. For the LMXB component, an absorbed PL model, with a photon index of 1.7 and an absorption column density of 10^{21} cm $^{-2}$, is adopted. For the CV+AB component, a fiducial spectral model based on the extended emission from M32 (Revnivtsev et al. 2007) is adopted. Specifically, we choose a two-temperature thermal plasma model (MEKAL+MEKAL in XSPEC), with temperatures of 0.38 and 4.6 keV and solar abundances. We note that this model is somewhat different from the MEKAL+PL model adopted by Revnivtsev et al. (2007), but preserves the idea that CVs and ABs typically exhibit soft and hard thermal spectra, respectively. We also note that the universality of the CV+AB emissivity is less certain at energies below 2 keV. In fact, M32 shows the lowest measured value of soft X-ray emissivity. Other measurements, such as those for NGC3379 and the M31 disk (Revnivtsev et al. 2008), yield a factor of 2 higher values, although the presence of soft X-ray-emitting gas cannot be completely ruled out in those two galaxies.

The stellar contribution in individual bands is thus determined and shown as curves in Fig. 5. It is immediately clear that stellar objects cannot fully account for the observed soft X-ray emission: *the expected stellar emission shows both a lower intensity and a smaller extent than the observed unresolved emission.* We therefore conclude the presence of truly diffuse emission arising from hot gas in and around the Sombrero bulge.

3.3.2. Truly diffuse X-ray emission

The 0.4-2 keV diffuse X-ray emission can then be obtained by subtracting the stellar component from the total unresolved emission (Fig. 4d). We construct radial intensity profiles for the diffuse emission in four quadrants of selected azimuthal ranges (Fig. 6), chiefly to examine deviations from symmetry. In Fig. 6a, the quadrants are defined to approximately follow the major- and minor-axes.

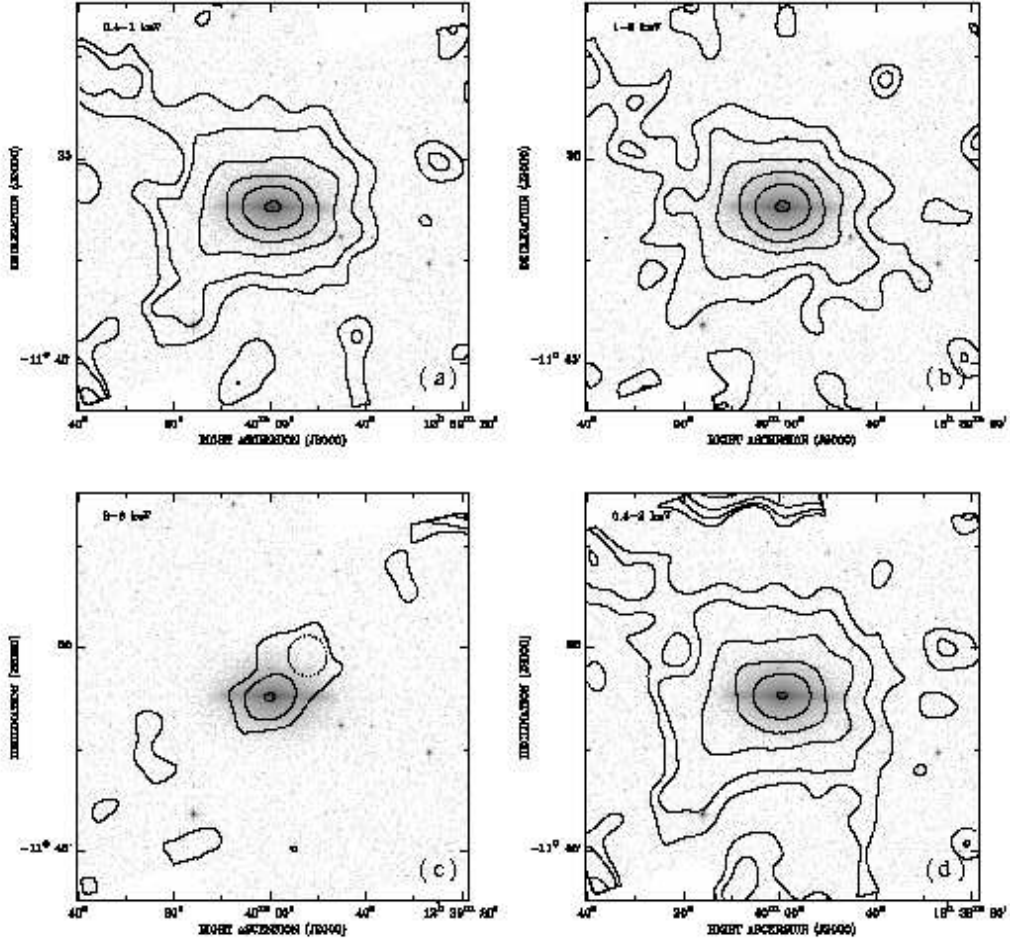


Fig. 4.— (a)-(c): 2MASS K-band image of Sombrero, overlaid by contours of the background-subtracted, exposure-corrected unresolved X-ray emission in the 0.4-1, 1-2 and 2-6 keV bands. The X-ray emission is smoothed by a Gaussian kernel of $\sigma=40''$ to bring up the faint extended emission. The dotted circle in (c) outlines the region where anomalous 2-6 keV signals are present. (d): the 0.4-2 keV diffuse X-ray emission, i.e., the contribution from unresolved stellar populations has been subtracted, overlaid on the 2MASS K-band image. The contour levels decrease by a factor of 2 in each step outward.

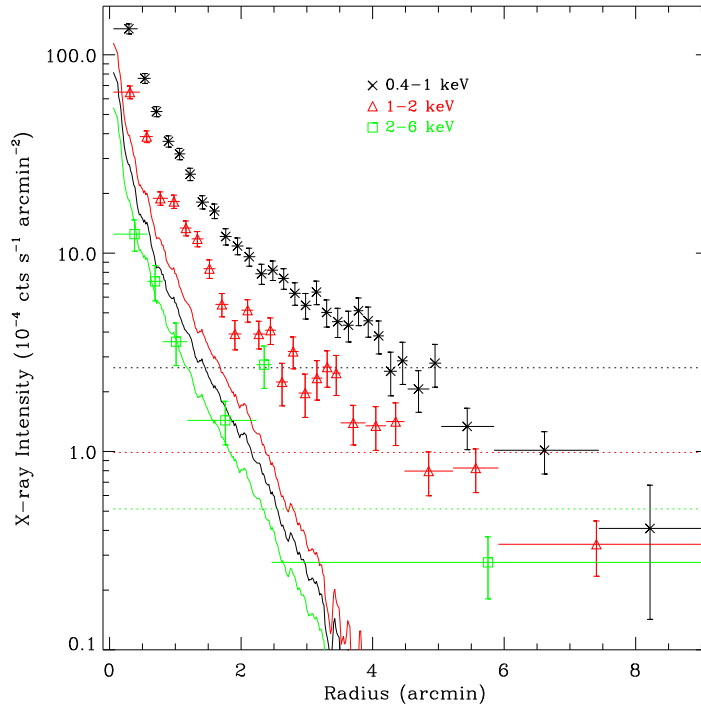


Fig. 5.— Azimuthally-averaged radial intensity distributions of the unresolved X-ray emission from Sombbrero, which are adaptively binned to achieve a signal-to-noise (with respect to the subtracted instrumental and sky background) ratio better than 4 and a minimum of 400 counts in each bin. Solid curves are normalized K-band intensity profiles, representing the combined contribution to individual bands from unresolved LMXBs, CVs and ABs. The dotted lines represent the level of the local sky background, effectively determined from regions beyond $R = 9'$. See text for details.

In the central $\sim 4'$, the diffuse emission appears stronger along the major-axis (i.e., azimuthal ranges of $[-30^\circ, 30^\circ]$ and $[150^\circ, 180^\circ]$) than along the minor-axis. In the innermost region, the emission appears faintest along the southern minor-axis (i.e., azimuthal ranges of $[210^\circ, 330^\circ]$), consistent with absorption by the dusty disk, the near side of which is tilted south. In Fig. 6b, the quadrants are defined as enclosed by a pair of the major- and minor-axes. In this configuration, the diffuse emission appears rather symmetric within the central $\sim 4'$, except it is fainter in the southern half of the innermost region, again presumably due to the absorption by the slightly tilted disk. At large radii (beyond $\sim 6'$), the emission appears stronger in the southeast, as suggested in Fig. 4.

A map of the hardness ratio of the diffuse emission, defined as $(I_{1-2 \text{ keV}} - I_{0.4-1 \text{ keV}})/(I_{1-2 \text{ keV}} + I_{0.4-1 \text{ keV}})$, is shown in Fig. 7. Interestingly, the emission appears softer along the disk region. To quantify this trend, we examine radial intensity profiles for the 0.4-1 and 1-2 keV diffuse emission in four quadrants, two of which sample the minor-axis and two along the major-axis. The profiles are shown in Fig. 8, along with the intensity ratio between the two bands in corresponding radial

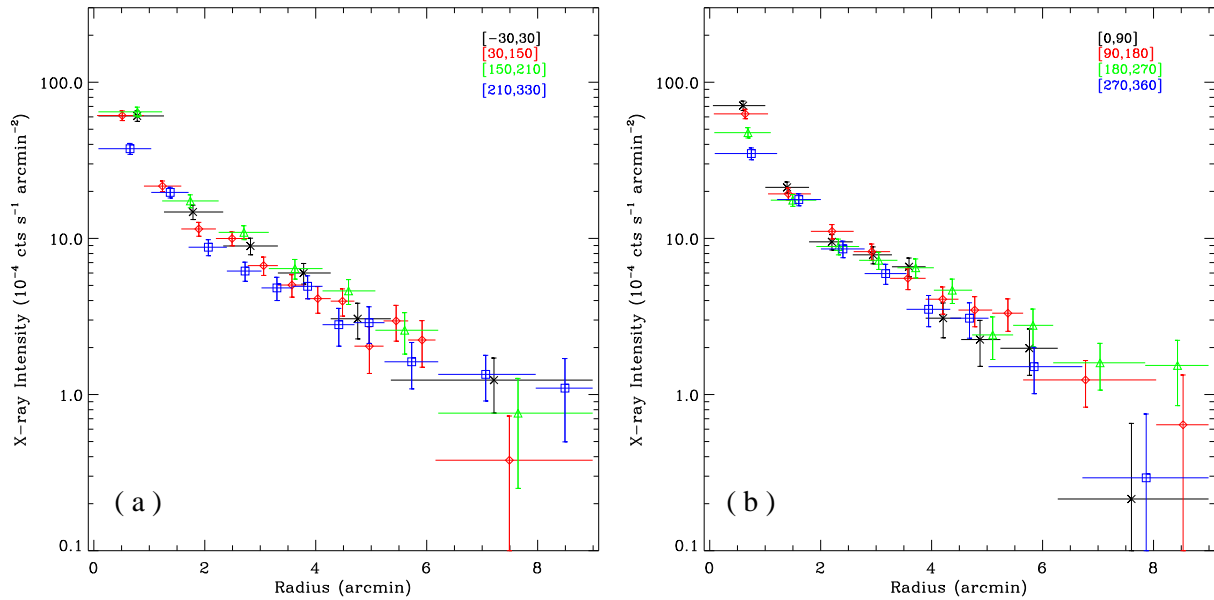


Fig. 6.— Azimuthally-averaged radial intensity profiles of the 0.4-2 keV diffuse emission, constructed from four quadrants and shown in different colors. The azimuthal ranges of the four quadrants are indicated in each panel. Angles are measured counterclockwise from the west, a direction assumed to be aligned with the major-axis of the disk. The profiles are binned to achieve a signal-to-noise (with respect to the combined stellar and background emission) better than 3 and a minimum of 900 counts per bin.

intervals. The two quadrants along the minor-axis clearly show softer emission in the central $\sim 2/5$.

3.4. Spectral properties of the hot gas

The new *Chandra* data allow us to carry out spatially-resolved spectral analysis of the diffuse emission. To trace the low-intensity emission to large radii, it is crucial to determine the local background, for which a “double-subtraction” procedure is used. Similar to the imaging analysis, a fiducial background is first considered, which includes the quiescent instrumental background, the PSF-scattered photons of the nucleus, the spatially non-uniform photons from unresolved sources, and the out-of-time events. In all the spectra analyzed below, such a fiducial background is subtracted.

It is then necessary to characterize the sky background, the spectra of which are extracted from regions beyond $R = 9'$ from both ObsID 9532 and 9533. We excluded discrete sources and avoided edges of the ACIS-I CCDs. We then use the *FTOOL addspec* to coadd the spectra obtained from the two observations and to generate averaged instrument responses (rmf and arf). Although

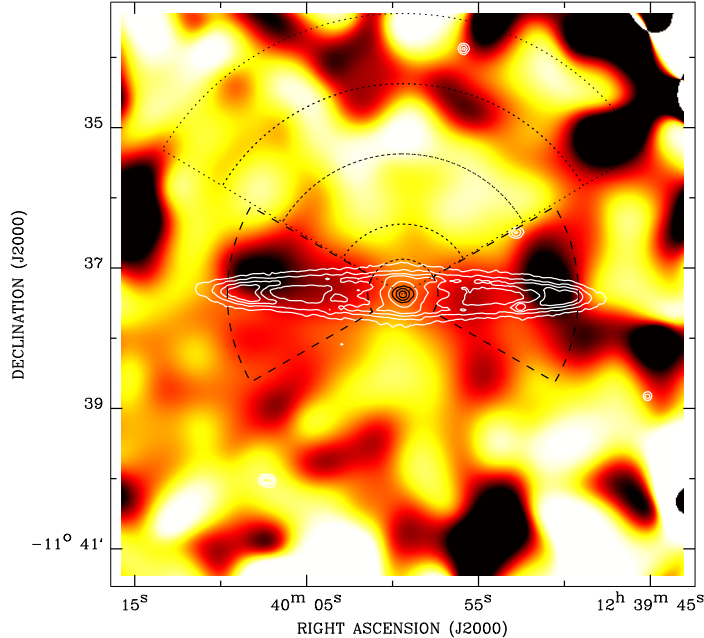


Fig. 7.— An image of the hardness of the diffuse emission, defined as $(I_{1-2 \text{ keV}} - I_{0.4-1 \text{ keV}})/(I_{1-2 \text{ keV}} + I_{0.4-1 \text{ keV}})$. Darker colors indicate lower values of hardness and hence softer emission. The contours show the *Spitzer*/*MIPS* $24 \mu\text{m}$ emission that traces the dust lane in the disk and the bright nucleus. The two dashed sectors define the disk region for spectral analysis, whereas the consecutive dotted sectors define inner bulge regions for spectral deprojection (see § 3.4).

these spectra sample different sky regions, such a procedure is warranted since the spectra were extracted from similar detector regions (hence the instrument response is similar). To maximize the statistics, we also extracted spectra from the S2 CCDs of the two observations, excluding obvious discrete sources, and similarly coadded the two spectra. The modeling of the sky background consists of three components. The first component is an absorbed PL, with a fixed photon index of 1.4 and a Galactic foreground absorption column density ($3.7 \times 10^{20} \text{ cm}^{-2}$), representing the unresolved cosmic AGNs (Moretti et al. 2003). The second component is a MEKAL model with a temperature of 0.1 keV, representing the emission from the Local Bubble and the Galactic halo. As noted by LWH07, the line of sight to Sombrero passes through the outskirts of the North Pole Spur (NPS; Willingale et al. 2003), a Galactic foreground soft X-ray-emitting feature. Hence a third component, another MEKAL, is added to characterize the NPS emission. Absorption to the two thermal components is allowed to vary below the Galactic foreground value, and a temperature of $0.27_{-0.03}^{+0.04}$ keV is found for the NPS, consistent with the findings of LWH07 and Willingale et al. (2003). In the following spectral fits, this model is adopted to account for the sky background,

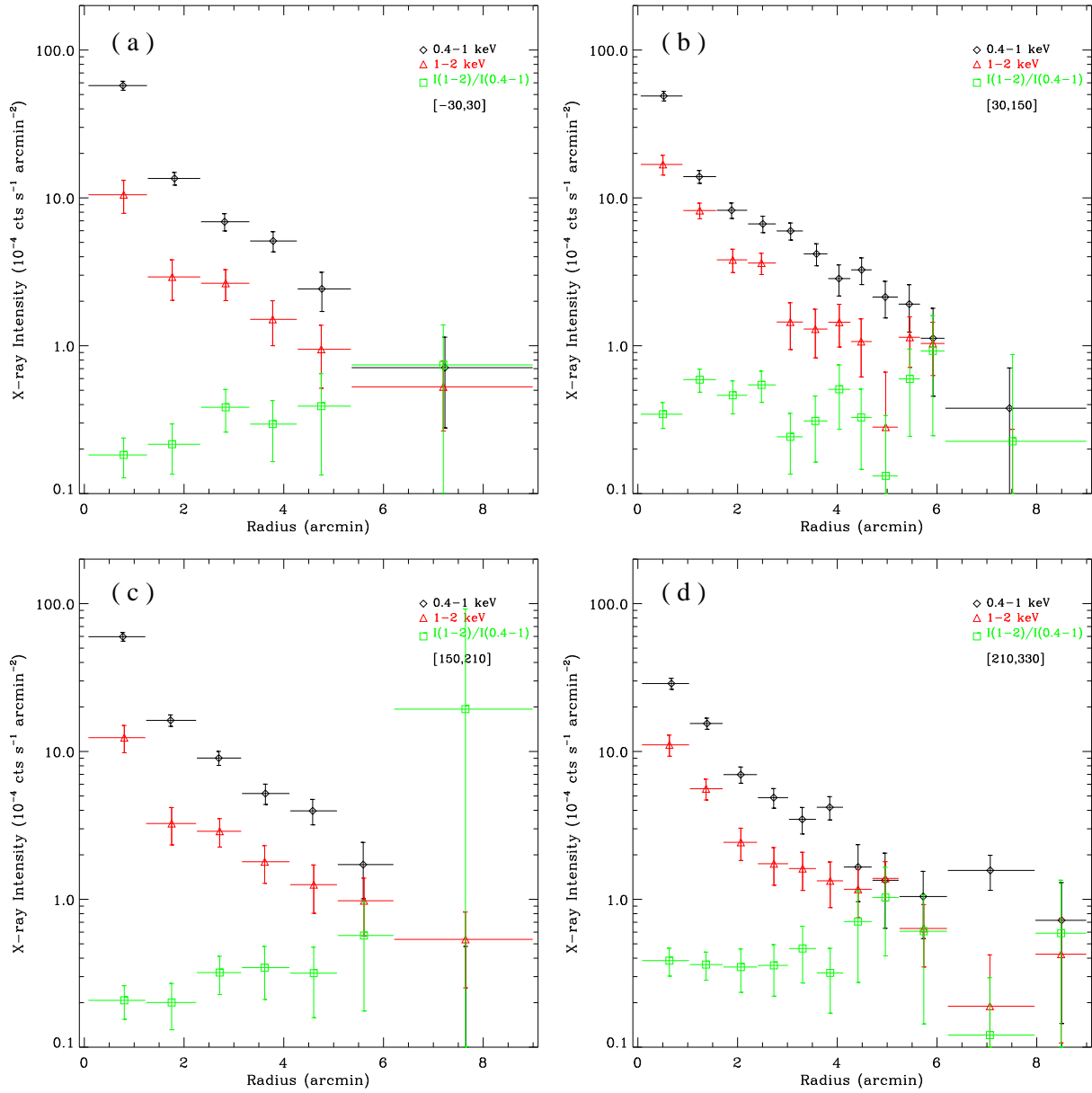


Fig. 8.— Azimuthally-averaged radial intensity profiles of the diffuse emission in the 0.4-1 (*black diamonds*) and 1-2 keV (*red triangles*) bands. Also shown are the intensity ratios between the two bands (*green squares*). The azimuthal range, within which the profile is constructed, is indicated in each panel. Angles are measured counterclockwise from west, a direction assumed to be aligned with the major-axis, i.e., the disk. The profiles are binned to achieve a signal-to-noise (with respect to the combined stellar and background emission) better than 3 and a minimum of 900 (0.4-2 keV) counts per bin.

with normalizations scaled to the underlying sky area.

Guided by the analysis in § 3.3, the diffuse emission appears softer along the disk, but otherwise shows no significant hardness variation in the outer regions. Hence we first consider two distinct regions, the disk and the bulge, chiefly to constrain the integrated spectral properties of the gas. The disk is defined by the two dashed sectors in Fig. 7, with inner-to-outer radii of $0'5$ - $2'5$ and azimuthal ranges of $\pm 30^\circ$ from the minor-axis. A disk spectrum is extracted for each of the three observations. The bulge is defined as the region outside the disk and within a radius of $5'$, where the field of view is common to ObsIDs 9532 and 9533. A bulge spectrum is extracted from each of these two observations. The disk and bulge spectra are then again coadded respectively with *addspec*.

We first characterize the bulge emission. In addition to the sky background, it is necessary to account for the stellar contribution. We adopt the spectral model derived for M32 to account for the CV+AB emission (MEKAL+MEKAL; § 3.3), with the normalizations scaled to the K-band light enclosed in the spectral extraction region. An additional PL, with a fixed photon index of 1.7, is adopted to account for the residual LMXB contribution. The normalization of this component is allowed to vary and is effectively constrained by the hard band photons. The stellar components are subject to the Galactic foreground absorption. We then characterize the diffuse gas by another MEKAL model, again subject to the Galactic foreground absorption. The fit is initiated by allowing the abundance, as a single value for different metals, to vary. An acceptable fit is obtained, giving a temperature of $0.58_{-0.04}^{+0.04}$ keV and an abundance of $2.2_{-0.8}^{+1.6}$, in the solar abundance standard of Grevesse & Sauval (1998). To test possible metal-enrichment processes, we group the metals into α elements (namely, C, N, O, Ne, Mg, Si, S, Ar and Ca) and non- α elements (namely, Na, Al, Fe and Ni). The abundance in each group is linked. At a temperature of ~ 0.6 keV, the Fe L-shell complex, clearly present in the bulge spectrum, is expected to have a dominating weight in constraining the overall abundance. Fixing the iron-like element abundance at a value of twice solar, the best-fit gives an α -to-Fe abundance ratio of $Z_\alpha/Z_{Fe} = 0.5_{-0.4}^{+0.5}$, marginally indicating that α elements are enriched to a lesser extent than iron, as expected if metal-enrichment is primarily from Type Ia supernovae (SNe Ia).

A similar fitting procedure is carried out for the disk emission. A MEKAL model for the gas gives a best-fit temperature of $0.40_{-0.05}^{+0.10}$ keV and a sub-solar ($0.2_{-0.1}^{+0.4}$) single abundance for all metals. When the metals are divided into two groups, the fitted Z_α/Z_{Fe} is $0.8_{-0.6}^{+0.7}$. While in the literature there have been arguments that a sub-solar abundance is unphysical given the metal-enrichment by evolved stars and is likely an artifact of fitting low spectral resolution CCD data to multi-temperature gas (e.g., Buote et al. 2003; Kim & Fabbiano 2003; David et al. 2010), there remains the possibility that the hot gas near the Sombrero disk is diluted by low-metallicity gas in the disk (see § 4). The fitted disk temperature is statistically lower than the bulge value, confirming the indication from hardness ratios (§ 3.3). The exact temperature of the disk-related gas can be even lower, as the disk spectrum inevitably includes the harder bulge emission from in front of the disk. To account for this effect, we add another MEKAL component to fit the disk

spectrum, whose temperature and abundance are fixed at 0.58 keV and 2 solar, respectively, to mimic the bulge emission. This results in a best-fit temperature of $0.33^{+0.13}_{-0.12}$ keV and an abundance of ~ 0.2 solar for the disk component. The fit results for the bulge and disk spectra are summarized in Table 2.

In what follows we characterize the thermal properties of the bulge gas using a spectral deprojection procedure. Bulge spectra are extracted from consecutive sectors, centering at the nucleus, with inner-to-outer radii of $0'-0'5$, $0'5-1'$, $1'-2'$, $2'-3'$, $3'-4'$, $4'-5'$, $5'-6'$ and $6'-9'$. For sectors within $4'$, the azimuthal range is chosen to be $\pm 60^\circ$ from the northern minor-axis (dotted regions in Fig. 7). These inner sectors are common to the field of view of all three observations. Hence a spectrum is extracted from each observation for each of these sectors, and spectra from the same sectors are coadded using *addspect*. Sectors outside $4'$ are essentially beyond the field of view of ObsID 1586, hence the correspondingly spectra are extracted from the other two observations. Paying attention to avoid CCD edges, we maximize the azimuthal range for these outer sectors, as the diffuse emission shows no significant azimuthal variation beyond $4'$, except in the outermost regions (Fig. 6).

We then apply the *projct* model in XSPEC to spectral deprojection. We account for the fact that only a fraction of the area within a given annulus is covered, due to the selected azimuthal range and source removal. A MEKAL model is adopted to characterize the diffuse emission, while the sky background and stellar emission are accounted for in the same way as for the above integrated bulge and disk spectra. Our primary goal here is to derive radial distributions of the gas temperature and density. Unfortunately the limited counting statistics do not allow us to examine a radial variation of the abundance. Hence we fix the abundance at 2 solar but allow the temperature to vary among different sectors. The resultant fit is found to be an adequate characterization of all the spectra. The derived radial distributions of gas temperature and density are shown in Fig. 9. The gas density has been converted from the MEKAL normalization, assuming a volume filling factor of unity. It is noteworthy that the derived gas density roughly inversely scales with the square root of the presumed abundance, since the spectrum of a ~ 0.6 keV gas is dominated by metal lines as long as the the abundance is near- or super-solar.

4. Discussion

Based on new *Chandra* data, we have confirmed LWH07’s detection of diffuse hot gas in and around the bulge of Sombrero. A key question to address is the origin and energetics of this gas. In principle, hot gas in and around galaxies can originate either externally from accretion of the IGM, or internally from stellar feedback processes such as stellar winds heated by supernova explosions. Feedback from an active nucleus, when it exists, can provide additional heating to the gas. We examine these possibilities in the following.

A generic prediction from current theories of galaxy formation is the presence of hot gaseous halos around present-day disk galaxies, which are the relic of accreted IGM heated to X-ray-

Table 1. Basic Information of Sombrero

Morphology ^a	SA(s)a
Center position ^a	R.A. 12 ^h 39 ^m 59 ^s .43
(J2000)	Dec. –11°37′23″.0
D_{25} ^a	8′.7 × 3′.5
Inclination angle ^b	84°
B-band magnitude ^a	8.98
V-band magnitude ^a	8.00
K-band magnitude ^a	4.96
Circular speed (km s ^{–1}) ^c	370
Distance (Mpc) ^d	9.0 ± 0.1
.....	(1′ ≅ 2.6kpc)
Redshift ^a	0.00342
Galactic foreground N_{HI} (10 ²⁰ cm ^{–2}) ^e	3.7

References. — ^aNED; ^bRubin et al. (1985); ^cBajaja et al. (1984); ^dSpitler et al. (2006); ^eDickey & Lockman (1990).

Table 2. Fits to the bulge and disk spectra^a

Parameter	Bulge		Disk		
	Mekal	FeMekal ^b	Mekal	FeMekal ^b	2Mekal ^c
$\chi^2/d.o.f.$	68.4/84	66.1/84	53.2/53	52.9/53	51.5/52
T (keV)	0.58 ^{+0.04} _{–0.03}	0.58 ^{+0.03} _{–0.02}	0.40 ^{+0.10} _{–0.05}	0.39 ^{+0.09} _{–0.06}	0.33 ^{+0.13} _{–0.12} /0.58
Z (Z_{\odot})	2.2 ^{+1.6} _{–0.8}	0.5 ^{+0.5} _{–0.4} ^d	0.2 ^{+0.4} _{–0.1}	0.8 ^{+0.7} _{–0.6} ^d	0.1 ^{+0.2} _{–0.1} /2
Norm (10 ^{–5})	4.4 ^{+3.8} _{–1.4}	4.9 ^{+0.4} _{–0.5}	9.1 ^{+6.2} _{–1.7}	9.1 ^{+0.8} _{–0.5}	9.6 ^{+25.5} _{–9.5} /0.4 ^{+0.5} _{–0.3}
Flux ^e	18.5	16.8	5.1	5.0	3.6/1.5

Note. — ^aOnly the model component for the diffuse gas is shown. See text for details on the sky background and stellar model components; ^bA Mekal model in which the abundance of α -elements is fit in terms of ratio to the iron abundance that is fixed at 2 solar; ^cTwo Mekal models; ^dFor the α -to-Fe abundance ratio; ^e0.3–2 keV unabsorbed flux in units of 10^{–14} ergs s^{–1} cm^{–2}.

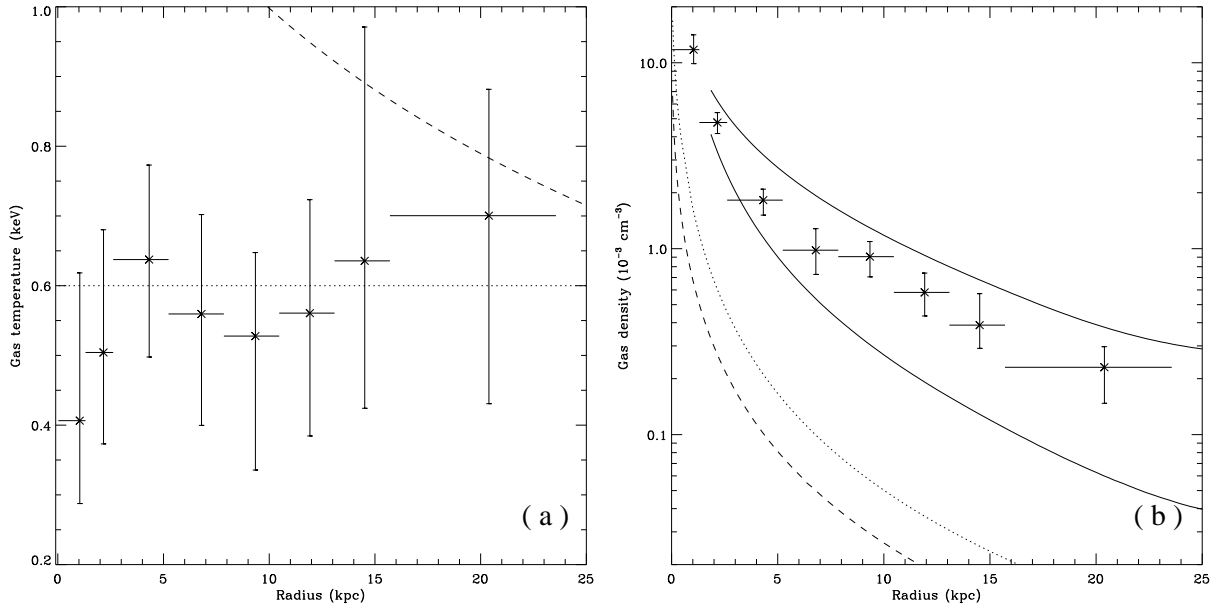


Fig. 9.— Radial distribution of gas temperature (a) and density (b) derived from spectral deprojection. The paired solid curves are the lower and upper bounds of the expected density distributions of an isothermal halo (with a fixed gas temperature of 0.6 keV) in hydrostatic equilibrium, based on the gravitational mass distribution of Bridges et al. (2007). The dashed curve represents the prediction of a steady, spherical wind with a specific heat ratio $\gamma = 5/3$, while the dotted curve is for an isothermal wind, i.e., $\gamma=1$. See the Appendix for details.

emitting temperatures, chiefly by accretion shocks and gravitational compression (White & Rees 1978; White & Frenk 1991). The development of such hot gaseous halos has been the subject of various recent hydrodynamical simulations (e.g., Toft et al. 2002; Rasmussen et al. 2009; Crain et al. 2010). These simulations generally find that the X-ray luminosity is a strong function of the gravitational mass of the host galaxy, as characterized by its circular rotation speed ($L_X \propto V_c^{5-7}$). With a maximum circular rotation speed $V_c \approx 370 \text{ km s}^{-1}$ (Bajaja et al. 1984), Sombrero is among the most massive disk galaxies in the local universe and hence may provide a strong constraint to this specific prediction of galaxy formation theories. LWH07 found that the amount of hot gas in the bulge/halo of Sombrero, with a measured X-ray luminosity of $\sim 3 \times 10^{39} \text{ ergs s}^{-1}$, is more than an order of magnitude lower than the value predicted by the simulations of Toft et al. (2002). Recently, Rasmussen et al. (2009) updated the Toft et al. simulations using a refined, higher-resolution treatment. They found that the detected amount of hot gas in Sombrero is comparable to their model prediction for a galaxy this massive. In an independent set of simulations by Crain et al. (2010), the predicted X-ray luminosities for Sombrero-like massive disk galaxies show a substantial scatter, whose lower bound is in agreement with the LWH07 measurement. From the above spectral analysis, we update the total 0.3-2 keV diffuse X-ray luminosity to be

$\sim 2.0 \times 10^{39}$ ergs s^{-1} . Hence an external origin of the hot gas in Sombrero cannot be ruled out on the basis of integrated X-ray luminosity. However, current numerical models typically lack a comprehensive treatment of internal feedback processes, such as nuclear and stellar feedback, which are expected to regulate the hot gaseous halo both mechanically and chemically. For instance, none of the Rasmussen et al. and Crain et al. simulations include nuclear feedback; these simulations implement the chemical feedback from SNe Ia, but either neglect or oversimplify their mechanical feedback. Nevertheless, the large population of old stars in Sombrero implies that SNe Ia and stellar mass-loss play an important role in shaping the observed diffuse X-ray emission. One such piece of evidence is the super-solar metal abundance inferred from the spectral fit (§ 3.4), which argues against the accreted IGM as a dominant origin of the bulge hot gas. Below we shall consider the internal feedback processes in Sombrero.

It is not trivial to trace and quantify the mechanical feedback from galactic nuclei. In particular, for those “inactive” nuclei showing a low radiation efficiency, much of the nuclear feedback is expected to be carried out (and/or accompanied) by jets of relativistic particles (e.g., Yuan et al. 2009). Allen et al. (2006) found an empirical relation between accretion rate and jet power in X-ray-bright elliptical galaxies, quantitatively as: $\log(L_{\text{Bondi}}/10^{43} \text{ ergs s}^{-1}) = 0.65 + 0.77 \log(L_{\text{jet}}/10^{43} \text{ ergs s}^{-1})$. The Bondi accretion rate of their sample nuclei ranges from $3.5 \times 10^{-4} M_{\odot} \text{ yr}^{-1}$ to $4.6 \times 10^{-2} M_{\odot} \text{ yr}^{-1}$, encompassing the value estimated for the nucleus in Sombrero (§ 3.2). This relation would imply a potential jet power of $\sim 1.4 \times 10^{42}$ ergs s^{-1} for Sombrero. In principle, this powerful nuclear feedback can result in cavities in the hot gaseous halo, especially along the direction of the kpc-scale linear radio structure found by Gallimore et al. (2006), but no such evidence is seen in our X-ray images. If the radio structure is truly jet-powered, an equipartition magnetic field strength of $B_{\text{eq}} \approx 4.5 \mu\text{G}$ can be inferred. To estimate this value, we have adopted the measured flux density of 3.1 mJy and length of $54''$ at 5 GHz (Gallimore et al. 2006) and assumed a canonical jet spectral index of 0.7 for the radio jet and a line-of-sight depth of $15''$ (limited by the image resolution). The corresponding magnetic field pressure, $\sim 8 \times 10^{-13}$ dyn cm^{-2} is ~ 10 times smaller than the thermal pressure of hot gas in the inner kpc ($\sim 8 \times 10^{-12}$ dyn cm^{-2}), but becomes comparable with the latter at radii beyond ~ 10 kpc. Interestingly, Fig. 4d and Fig. 6 suggest an elongation along the direction of the radio structure (i.e., toward southeast) in the diffuse X-ray emission which otherwise appears rather symmetric. This may be the site where the assumed jet becomes dynamically important to the hot gas. The mechanical energy deposited by the jet can be characterized by the PV work, $\sim 2.2 \times 10^{53}$ ergs, if we adopt the thermal pressure instead of the smaller equipartition magnetic field pressure. The timescale for this energy to be consumed by the gas is rather uncertain. If we assume that the jet grows to the observed size at the sound speed of the hot gas, we estimate a timescale of 2.8 Myr and hence an average mechanical heating rate of 1.2×10^{39} ergs s^{-1} . Similarly, if the circumnuclear X-ray/optical line feature (§ 3.2) is powered by the jet, a heating rate of $\sim 10^{39}$ ergs s^{-1} can be inferred. These heating rates, while being comparable to the observed X-ray luminosity of the hot gas, are much less than the integrated heating rate by SNe Ia, as we shall show below. They also suggest a rather inefficient extraction of the possible jet power. In principle, the nuclear feedback may cause distinct effects

in the circumnuclear ISM, e.g., a steep pressure gradient (e.g., Bland-Hawthorn 1995). At present, probing such an effect is however hampered by the bright X-ray nucleus and the lack of suited optical spectroscopic observations.

The most violent form of stellar feedback is related to massive stars (cf. Veilleux, Cecil & Bland-Hawthorn 2005). Hot gas heated by stellar winds and core-collapse Type II SNe is commonly detected in active star-forming galaxies with an edge-on disk perspective (e.g., Strickland et al. 2004; Tullmann et al. 2006; Li et al. 2008). Low level star formation is likely present in the disk of Sombrero. $H\alpha$ emission and radio continuum emission are detected along the disk (LWH07; Bajaja et al. 1988), both implying a star formation rate (SFR) of $\sim 0.1 - 0.2 M_{\odot} \text{ yr}^{-1}$. Using the L_X -SFR relation found by Strickland et al. (2004) and Li et al. (2008), a 0.3-2 keV luminosity of $(2-8) \times 10^{37} \text{ ergs s}^{-1}$ is expected. Compared to the measured diffuse X-ray luminosities along the disk and in the bulge (Table 2), we conclude that star-forming activities contribute little to the detected diffuse X-ray emission in Sombrero, although their mechanical input to the hot gas cannot be ruled out.

Lastly, we consider feedback from old stellar populations. Empirically, the old stars in a galactic bulge continuously deposit energy and mass into the interstellar medium (ISM) at rates of $\sim 1.1 \times 10^{40} [L_K / (10^{10} L_{K,\odot})] \text{ ergs s}^{-1}$ and $\sim 0.02 [L_K / (10^{10} L_{K,\odot})] M_{\odot} \text{ yr}^{-1}$ (e.g., Mannucci et al. 2005; Knapp, Gunn & Wynn-Williams 1992; see also Appendix), respectively, where L_K is the K-band luminosity of the bulge. A “missing stellar feedback” problem is often found in gas-poor, i.e., low L_X/L_K , early-type galaxies, where the X-ray luminosity, mass and metal content of the hot gas inferred from observations account for only a small fraction of the expected stellar feedback (e.g., O’Sullivan, Ponman & Collins 2003; David et al. 2006; LWH07; Li & Wang 2007; Wang 2010). Sombrero, with $L_X/L_K \sim 10^{28} \text{ ergs s}^{-1} / 10^{10} L_{K,\odot}$, shows such a discrepancy. From the spectral analysis we have measured $L_X \approx 2.0 \times 10^{39} \text{ ergs s}^{-1}$ and $M_{\text{gas}} \approx 2.9 \times 10^8 M_{\odot}$, whereas the expected SNe Ia heating rate is $\sim 2.2 \times 10^{41} \text{ ergs s}^{-1}$ and the expected mass input rate is $\sim 0.4 M_{\odot} \text{ yr}^{-1}$ (taking only $\sim 7 \times 10^8 \text{ yr}$ to accumulate the observed amount of hot gas). We note that the mass input rate is several times higher than the rate of on-going star formation on the disk, and that the mass of cold gas in both the disk and the bulge is no more than a few $10^8 M_{\odot}$ (Bajaja et al. 1984; Matsumura & Seki 1989; after rescaling the adopted distances therein), together indicating that the bulk of mass returned by the old stars is unlikely to be stored within where it is produced. Naturally, the energy and mass discrepancies can be explained with the presence of an outflow of hot gas, through which the “missing” energy and mass are transported outside the regions covered by the observations. Such an outflow is expected to show distinct thermal structures, i.e., the radial distributions of gas temperature and density.

Indeed, with its diffuse X-ray emission being traced to at least $\sim 23 \text{ kpc}$ from the center, Sombrero is an ideal target for examining the thermal structures. The simplest case is that the hot gas is in hydrostatic equilibrium with the gravitational potential. The predicted density distribution for an isothermal gas halo, as implied by the nearly constant gas temperature, is shown as solid curves in Fig. 9. The gravitational potential distribution is obtained by modeling the observed

kinematics of globular clusters out to a radius of ~ 25 kpc (Bridges et al. 2007). Within the current uncertainties in both the X-ray and kinematic data, the observed density distribution is consistent with a hydrostatic equilibrium case. However, as stars would continuously return mass to the interstellar space, a hydrostatic gas halo is expected to increase its mass at the rate of integrated mass input given above, which is not observed. We note that the gas mass fraction, with respect to the gravitational mass, is only $\sim 0.3\%$ within a radius of 25 kpc. Again, this indicates that Sombrero is losing its hot gas.

To examine the gas temperature and density distributions regulated by feedback from old stellar populations, we construct a simple one-dimensional hydrodynamic model (cf. Appendix for details) for a galactic-scale transonic wind. The results are shown as dashed and dotted curves in Fig. 9. Clearly, the wind density drops rapidly as the result of outward expansion, being ~ 10 times lower than the observed value at radii beyond 10 kpc. The corresponding X-ray luminosity is more than 100 times lower than the observed value. We note that the adopted spherical symmetry in our model is practically simplified, in view of Sombrero’s starlight distribution. The shape of the gravitational potential in the inner few arcminutes, in particular, is regulated by the ellipsoidal bulge and the disk. Moreover, gas returned by the evolved stars may carry a net angular momentum due to the rotation of the bulge. The flattening and rotation of stars may conspire to modify the dynamics of the hot gas and hence its morphology (e.g., Ciotti & Pellegrini 1996; D’Ercole & Ciotti 1998). This is hinted at by the boxy morphology of the diffuse emission in the inner regions (Fig. 4). Nevertheless, the importance of such an effect is expected to decrease with radius, and any resultant increase in the amount of hot gas is unlikely sufficient to account for the observed discrepancy by a factor of ~ 100 , without producing an even greater amount of cold gas in the disk (D’Ercole & Ciotti 1998). A detailed modeling of a flattened, rotating outflow is beyond the scope of the present work.

An alternative, qualitatively viable solution is that the hot gas forms a subsonic outflow (e.g., David, Forman & Jones 1991; Tang et al. 2009a), the thermal structure of which still resembles, and hence is difficult to distinguish from, a quasi-hydrostatic halo, especially at large radii. This can be seen by estimating the asymptotic flow velocity $V_g = \dot{M}/(4\pi R^2 \mu m_H n_g)$. Adopting the measured gas density (n_g) at the outermost radius (~ 20 kpc; Fig. 9) and the total mass outflowing rate (\dot{M}) of $0.4 M_\odot \text{ yr}^{-1}$ (i.e., the collective mass loss from the old stars), we have $V_g \approx 20 \text{ km s}^{-1}$, which is much less than the local sound speed. Recent numerical simulations of bulge outflows indicate that the thermal structures are time-dependent and sensitively depend on the formation history and environment of the host galaxy (Tang et al. 2009a). Interestingly, the simulations predict that the effective temperature of the outflow is relatively low in the central region, chiefly due to the non-uniform thermalization of the SNe Ia energy in a dense environment (Tang et al. 2009b). The low gas temperature near the disk of Sombrero seems to be consistent with this prediction. In addition, thermal conduction and/or charge exchange between the hot gas and the cold gas residing in the disk may lead to softer X-ray emission, a situation suggested to be present in the circumnuclear region of M31 (Li, Wang & Wakker 2009; Liu et al. 2010).

Another possibility is that the observed soft X-rays arise from the interfaces between a very hot (a few keV) wind and an entrained, cold medium (see e.g., Veilleux et al. 2005). In this case, the wind temperature would be consistent with the empirical specific energy input per gas particle from evolved stars. However, the current X-ray data of Sombrero provide no compelling evidence for such a wind, e.g., in terms of diffuse hard X-ray emission and/or iron K-shell lines as observed in the superwind galaxy M82 (Strickland & Heckman 2007). On the other hand, extraplanar cold gas can be probed as extinction features against the bulge starlight (e.g., Howk & Savage 1997, 1999; Li et al. 2009). We find no such evidence in *HST* broad-band optical images of Sombrero.

5. Summary

Based on new and archival *Chandra* observations, we have studied the X-ray nucleus and the diffuse hot gas in the bulge-dominated, edge-on, Sa galaxy Sombrero. The study can be summarized as follows:

1. The 0.3-8 keV luminosity of the nucleus appears to be constant at $\sim 2.4 \times 10^{40}$ ergs s⁻¹ on three epochs between December 1999 and April 2008, but drops by a factor of two in the November 2008 observation. The observed X-ray luminosity is only one part in 10^7 of the *Eddington* luminosity for the SMBH, characteristic of a radiatively inefficient accretion flow. No significant spectral variation is found associated with the flux change. The nuclear spectrum can be characterized by a power-law with a photon index of ~ 2 and a moderate absorption column density of $\sim 3 \times 10^{21}$ cm⁻².

2. After properly accounting for the contribution of unresolved stellar sources, in particular CVs and ABs whose quasi-universal X-ray emissivity is recently established, we isolate the truly diffuse emission of hot gas. The extent of this diffuse emission is significantly larger than that of the star light, reaching a galactocentric radius of at least 23 kpc, where it becomes indistinguishable from the local sky background.

3. The hot gas shows a temperature of ~ 0.6 keV with little statistically significant variation across the field of view, except around the disk where a lower temperature of ~ 0.3 keV is hinted. This cooler gas may result from thermal conduction and/or turbulent mixing with the cold ISM in the disk.

4. While the total intrinsic luminosity of the hot gas is comparable to the prediction by the latest galaxy formation models, in which a hot gaseous halo is a generic feature of a disk galaxy formed by the accretion of the IGM, we show that the role of internal feedback processes, in particular the energy input by SNe Ia and the mass input by evolved stars, cannot be neglected.

5. A simple hydrodynamic model characterizing the stellar feedback and the gravitational potential in Sombrero, in which the hot gas is in the form of a supersonic wind, however, fall far short of reproducing the observed amounts of X-ray luminosity and gas mass. While recent more sophisticated numerical simulations suggest that a subsonic outflow is a viable solution,

understanding of the thermodynamical structure of the hot gas in Sombrero and in other typically intermediate-mass early-type galaxies continues to be pursued.

ZL is grateful to the useful comments and discussions with Robert Crain, Larry David, Hui Dong and Dan Harris. This work is supported by the SAO grant G08-9088.

A. A Galactic Wind Model

Hydrodynamic models for galactic-scale flows have long been developed (e.g., Mathews & Baker 1971; White & Chevalier 1983, 1984; Loewenstein & Mathews 1987; David, Forman & Jones 1990; Ciotti et al. 1991), most of which are in the scope of elliptical galaxies for which spherical symmetry is a reasonable approximation. The essence of these models includes the characterization of the gravitational potential and the mass and energy deposition (i.e., stellar feedback) to the gas flow. Such properties, which together determine the gas dynamics, are practically difficult to constrain from direct observations. Our approach is to construct a model with simple, but essential physical considerations, aiming to confront the modeled gas properties with observational results.

A.1. Physical assumptions and formulation

Our first assumption is that the gas flow is in a steady state and a spherical symmetry. The dynamical timescale of a wind is much shorter than the timescale of galaxy evolution, hence it is reasonable to assume that the mass and energy input from evolved stars, which together supply the gas flow, are at constant rates. Spherical symmetry is not only a practical assumption, as used in most theoretical models, but also is supported in the X-ray morphologies of galactic spheroids. All physical parameters considered hereafter, e.g., gas density and temperature, are functions of galactocentric radius. Second, we assume that the mass and energy input spatially follow the distribution of stars. The mass input is essentially contributed by the ejecta of evolved stars, such as stellar winds and planetary nebulae; the energy input is primarily provided by mechanical energy from Type Ia SNe, with additional orbital energy carried by the stellar ejecta.

In galaxies where gas outflows exist, the X-ray luminosity is typically as low as only a few percent of the energy input. Thus we neglect the effect of radiative cooling on the gas dynamics. This is a good approximation as the cooling timescale is much longer than the dynamical timescale, probably except for the central region. Other assumptions that have been made include neglecting thermal conduction, viscosity, and self-gravity of the gas.

Now the physical properties of the gas can be described by the hydrodynamic equations:

$$\frac{1}{r^2} \frac{d}{dr} (\rho u r^2) = \dot{m}(r), \quad (\text{A1})$$

$$\rho u \frac{du}{dr} = -\frac{dP}{dr} - \rho g - \dot{m}(r)u, \quad (\text{A2})$$

$$\frac{1}{r^2} \frac{d}{dr} [\rho u r^2 (\frac{1}{2} u^2 + \frac{\gamma}{\gamma-1} \frac{P}{\rho})] = -\rho g u + \dot{E}(r), \quad (\text{A3})$$

where u , ρ , and P are the velocity, density and pressure of gas, respectively. γ is the ratio of specific heats. $g(r)$ is the gravitational force given by

$$g(r) = \frac{G[M_s(r) + M_d(r)]}{r^2}, \quad (\text{A4})$$

$$M_s(r) = \int_0^r 4\pi \rho_s(r) r^2 dr, \quad (\text{A5})$$

$$M_d(r) = \int_0^r 4\pi \rho_d(r) r^2 dr, \quad (\text{A6})$$

where $\rho_s(r)$ and $\rho_d(r)$ are the density distributions of stellar mass and dark matter, respectively. $\dot{m}(r)$ and $\dot{E}(r)$ are the mass and energy input rates per unit volume, which are assumed to be proportional to the density of stellar mass $\rho_s(r)$.

A.2. Galaxy modeling

A valid solution of the above hydrodynamic equations stands on a specific realization of the host galaxy, i.e., the spatial distributions of stars and dark matter and the mass and energy input rates from stars. To derive the spatial distribution of stars, we deproject a de Vaucouleurs’s law, which is empirically used to describe the stellar surface brightness profile of elliptical galaxies and bulges. We adopt an effective radius $R_e = 105''$ (~ 4.6 kpc) for the bulge of Sombrero (Bendo et al. 2006). We note that the stellar disk contributes less than 20% of the total stellar mass in Sombrero and is neglected. The total stellar mass M_{st} , $1.5 \times 10^{11} M_\odot$, is determined from the color-dependent mass-to-light ratio of Bell et al. (2003) based on the 2MASS K-band luminosity of Sombrero. For the dark matter halo, we adopt the NFW profile (Navarro, Frenk and White 1996),

$$\rho_d(r) = \frac{\rho_{d0}}{\frac{r}{r_d} (1 + \frac{r}{r_d})^2}. \quad (\text{A7})$$

ρ_{d0} can be replaced by an algebraic combination of the total dark matter mass M_{dt} and the concentration parameter $C \equiv R_v/r_d$. The galaxy boundary is defined to be the virial radius, R_v , which scales with the cube root of the virial mass (total mass of stars and dark matter). Since we have good observational constraints on the distributions of stellar mass (based on K-band light) and gravitational mass (based on kinematics of globular clusters out to $r=25$ kpc; Bridges et al. 2007), we fit the NFW profile to the difference between the gravitational mass and the stellar mass to obtain $r_d=27$ kpc, $R_v=483$ kpc and $M_{dt}=6.8 \times 10^{12} M_\odot$.

To complete the modeling, we also need to specify the total stellar mass loss rate \dot{m}_0 and the collective energy input rate \dot{E}_0 , so as to determine $\dot{m}(r)$ and $\dot{E}(r)$ (both assumed to be proportional

to ρ_s) via relations

$$\int_0^{R_v} 4\pi r^2 \dot{m}(r) dr = \dot{m}_0, \quad (\text{A8})$$

$$\int_0^{R_v} 4\pi r^2 \dot{E}(r) dr = \dot{E}_0. \quad (\text{A9})$$

\dot{m}_0 and \dot{E}_0 are the two key parameters in our model.

For a given galaxy, there are also empirical methods to estimate \dot{m}_0 and \dot{E}_0 . Knapp, Gunn and Wynn-Williams (1992) suggested the following relation as a direct measurement of the current mass loss rate from evolved stars in elliptical galaxies, using the 2.2 μm flux density

$$\dot{m} = 8 \times 10^{-4} \left(\frac{D}{\text{Mpc}}\right)^2 \left(\frac{S_{2.2}}{\text{Jy}}\right) M_\odot \text{ yr}^{-1} = 0.02 \times 10^{-2} \left(\frac{L_K}{10^{10} L_{\odot,K}}\right) M_\odot \text{ yr}^{-1}. \quad (\text{A10})$$

The energy input consists of that from Type Ia SNe and that from stars, i.e., $\dot{E}_0 = \dot{E}_{0,\text{SN}} + \dot{E}_{0,\text{star}}$. By assuming a typical released energy of 10^{51} ergs for a single SN explosion,

$$\dot{E}_{0,\text{SN}} = 1.1 \times 10^{40} \left(\frac{R_{\text{SN}}}{0.035 \text{ SNUK}}\right) \left(\frac{L_K}{10^{10} L_{\odot,K}}\right) \text{ ergs s}^{-1}, \quad (\text{A11})$$

where R_{SN} is the observed Type Ia SNe rate in units of SNUK (one per $10^{10} L_{\odot,K}$ per 100 yr) for early-type galaxies at low redshifts (Mannucci 2005).

The stellar ejecta also carry mechanical energy obtained from the orbital motion of the progenitor star,

$$\dot{E}_{0,\text{star}} = \frac{1}{2} \dot{m}_0 \sigma^2 \approx 0.6 \times 10^{39} \left(\frac{L_K}{10^{10} L_{\odot,K}}\right) \left(\frac{\sigma}{300 \text{ km s}^{-1}}\right)^2 \text{ ergs s}^{-1}, \quad (\text{A12})$$

where σ is the stellar velocity dispersion. Clearly, $\dot{E}_{0,\text{SN}}$ is the dominant form of energy input.

Closely relevant is the metal-enrichment of gas predominantly by the SNe. We take the iron enrichment as an example. Nomoto, Thielemann and Yokoi (1984) calculated the Fe yield per Type Ia SN to be $0.7 M_\odot$, about half of the total released mass. Assuming a complete mixture of the iron atoms with the gas, the iron abundance can be estimated as

$$Z_{\text{Fe}} = Z_{\text{Fe,star}} + 9.7 \left(\frac{3.16 \times 10^{-5}}{[n_{\text{Fe}}/n_{\text{H}}]_\odot}\right) \left(\frac{R_{\text{SN}}}{0.035 \text{ SNUK}}\right), \quad (\text{A13})$$

which is independent of the total stellar content. According to Grevesse & Sauval (1998), $[n_{\text{Fe}}/n_{\text{H}}]_\odot = 3.16 \times 10^{-5}$, thus by assuming that $Z_{\text{Fe,star}}$ equals solar, Eq.(A13) gives $Z_{\text{Fe,gas}} = 10.7$.

A.3. Solution

To solve Eqs.(A1) - (A3), three boundary conditions, or three equivalent constraints on the variables, are generally needed. Given a natural assumption that the gas velocity is zero at the

center, we have the first boundary condition,

$$u|_{r=0} = 0. \quad (\text{A14})$$

With a further assumption that the derivatives of velocity and temperature are finite at the center, Eq.(A3) and (A14) require that

$$kT_0 \equiv kT|_{r=0} = \mu_g m_H \frac{P}{\rho}|_{r=0} = \mu_g m_H \frac{\gamma - 1}{\gamma} \frac{\dot{E}_0}{\dot{m}_0}, \quad (\text{A15})$$

where μ_g is the mean molecular weight of gas taken to be 0.6, m_H and k have the conventional meanings.

Now it is convenient to introduce a dimensionless variable, the Mach number $M \equiv u/c_s$, where $c_s \equiv (\gamma P/\rho)^{1/2}$ is the sound speed of gas. With Eq.(A14) and (A15), one can show that equations (A1)-(A3) reduce to a first order differential equation of the Mach number

$$\begin{aligned} \frac{dM^2}{dr} &= \frac{M^2}{M^2 - 1} \left(1 + \frac{\gamma - 1}{2} M^2\right) g(r, M), \\ g(r, M^2) &= \frac{4}{r} - \frac{\gamma + 1}{\gamma - 1} \frac{\frac{dW}{dr}}{L - W} - (1 + \gamma M^2) \left[\frac{\frac{dF}{dr}}{F} + \frac{\frac{dL}{dr}}{L - W}\right], \end{aligned} \quad (\text{A16})$$

where

$$F(r) = \int_0^r 4\pi \dot{m}(r) r^2 dr, \quad (\text{A17})$$

$$L(r) = \int_0^r 4\pi \dot{E}(r) r^2 dr, \quad (\text{A18})$$

$$W(r) = \int_0^r F(r) \frac{d\phi}{dr} dr. \quad (\text{A19})$$

In general the right-hand side of Eq.(A16) is singular when $M = 1$. Correspondingly, the radius $r = r_c$ at which $M = 1$ is called the *sonic radius* or *critical radius*. A wind solution requires that the gas flow smoothly passes through the sonic radius. This provides a third boundary condition to the solution,

$$g(r, M)|_{r_c} = 0, \quad (\text{A20})$$

so that the right-hand side of Eq.(A16) remains regular when $M = 1$.

To derive the wind solution, the location of the sonic radius is first found by solving Eq.(A20), which is simply an algebraic equation of r . Then *L'Hospita's* rule is applied to obtain the derivative of M at r_c . Finally, a wind solution is found by integrating Eq.(A16) starting from r_c inward to the center and from outward to the virial radius. An adaptively stepping fifth order Runge-Kutta method is used when performing the numerical solution.

REFERENCES

- Allen S.W., Dunn R.J.H., Fabian A.C., Taylor G.B., Reynolds C.S. 2006, MNRAS, 372, 21
- Bajaja E., Hummel E., Wielebinski R., Dettmar R.-J., 1988, A&A, 35
- Bell E.F., McIntosh D.H., Katz N., Weinberg M.D. 2003, ApJS, 149, 289
- Bendo G.J., et al. 2006, ApJ, 645, 134
- Bianchi S., Guainazzi M., Chiaberge M. 2006, A&A, 448, 499
- Bland-Hawthorn J. 1995, PASA, 12, 190
- Bogdán Á., & Gilfanov M. 2008, MNRAS, 388, 56
- Bondi H. 1952, MNRAS, 112, 195
- Bridges T.J., Rhode K.L., Zepf S.E., Freeman K.C. 2007, ApJ, 658, 980
- Buote D.A., Lewis A.D., Brighenti F., Mathews W.G. 2003, ApJ, 595, 151
- Ciotti L., D’Ercole A., Pellegrini S., Renzini A. 1991, ApJ, 376, 380
- Ciotti L., Pellegrini S. 1996, MNRAS, 279, 240
- Crain R.A., McCarthy I.G., Frenk C.S., Theuns T. 2010, MNRAS, 407, 1403
- David L.P., Forman W., Jones C. 1990, ApJ, 359, 29
- David L.P., Forman W., Jones C. 1991, ApJ, 380, 39
- David L.P., Jones C., Forman W. Vargas I.M., Nulsen P. 2006, ApJ, 653, 207
- David L.P. et al. 2010, ApJ submitted (arXiv:1010.0650)
- Davis J.E. 2001, ApJ, 562, 575
- D’Ercole A., & Ciotti L. 1998, ApJ, 494, 535
- Dickey J.M., Lockman F.J. 1990, ARA&A, 28, 215
- Diehl S., & Statler T.S. 2007, ApJ, 668, 150
- Di Stefano R., Kong A.K.H., Van Dalfsen M.L., Harris W.E., Murray S. S., Delain K.M., 2003, ApJ, 599, 1067
- Ellis S.C., & O’Sullivan E. 2006, MNRAS, 367, 627
- Emsellem E., & Ferruit P. 2000, A&A, 357, 111
- Fabbiano G., & Juda J.Z. 1997, ApJ, 476, 666
- Forman W., Jones C., Tucker W. 1985, ApJ, 293, 102
- Fukazawa Y., Botoya-Nonesca J.G., Pu J., Ohto A., Kawano N. 2006, ApJ, 636, 698
- Gallimore J.F., Axon D.J., O’Dea C.P., Baum S.A., Pedlar A. 2006, ApJ, 132, 546
- Gallo E., Treu T., Marshall P.J., Woo J.-H., Leipski C., Antonucci R. 2010, ApJ, 714, 25
- Gilfanov M. 2004, MNRAS, 349, 146

- Grevesse N., Sauval A. J., 1998, *Space Sci. Rev.*, 85, 161
- Heckman T.M. 1980, *A&A*, 87, 152
- Ho L.C., Filippenko A.V., Sargent W.L.W. 1997, *ApJS*, 112, 315
- Howk J.C., Savage B.D. 1997, *AJ*, 114, 2463
- Howk J.C., Savage B.D. 1999, *AJ*, 117, 2077
- Irwin J.A., Sarazin, C.L., Bregman J.N. 2002, *ApJ*, 570, 152
- Jarrett T.H., Chester T., Cutri R., Schneider S.E., Huchra J.P., 2003, *AJ*, 125, 525
- Kennicutt R.C.Jr. 1998, *ARA&A*, 36, 189
- Kim D.-W., Fabbiano G. 2003, *ApJ*, 586, 826
- Knapp G.R., Gunn J.E., Wynn-Williams C.G., 1992, *ApJ*, 399, 76
- Kormendy J. 1988, *ApJ*, 335, 40
- Kormendy J. et al. 1996, *ApJ*, 473, L91
- Lanz L., Jones C., Forman W.R., Ashby M.L.N., Kraft R., Hickox R.C. 2010, *ApJ*, 721, 1702
- Li J.-T., Li Z., Wang Q.D., Irwin J.A., Rossa J., 2008, *MNRAS*, 390, 59
- Li J.-T., Wang Q.D., Li Z., Chen Y. 2009, *ApJ*, 706, 693
- Li Z., Wang Q.D, Hameed S. 2007 *MNRAS*, 376, 960 (LWH07)
- Li Z. & Wang Q.D., 2007, *ApJ*, 668, L39
- Li Z., Wang Q.D., Wakker B.P. 2009, *MNRAS*, 397, 148
- Li Z. et al. 2010, *ApJ*, 721, 1368 (Paper I)
- Liu J., Wang Q.D., Li Z., Peterson J.R. 2010, *MNRAS*, 404, 1879
- Loewenstein M. & Mathews W. 1987, *ApJ*, 319, 614
- MacArthur L.A., González J.J., Courteau S. 2009, *MNRAS*, 395, 28
- Mannucci F., Della Valle M., Panagia N., Cappellaro E., Cresci G., Maiolino R., Petrosian A., Turatto M., 2005, *A&A*, 433, 807
- Markevitch M. et al. 2000, *ApJ*, 541, 542
- Masegosa J., Márquez I., Ramirez A., González-Martín O. 2010, *A&A*, in press
- Mathews W.G. & Baker J.C. 1971, *ApJ*, 170, 241
- Matsumura M. & Seki M. 1989, *A&A*, 209, 8
- Memola E., Trinchieri G., Wolter A., Focardi P., Kelm B. 2009, *A&A*, 497, 359
- Moretti A., Campana S., Lazzati D., Tagliaferri G., 2003, *ApJ*, 588, 696
- Navarro J.F., Frenk C.S., & White S.D.M., 1996, *ApJ*, 462, 563

- Nicholson K.L., Reichert G.A., Mason K.O., Puchnarewicz E.M., Ho L.C., Shields J.C., Filippenko A.V. 1998, MNRAS, 300, 893
- O’Sullivan E., Forbes D.A., Ponman T.J. 2001, MNRAS, 328, 461
- O’Sullivan E., Ponman T.J., Collins R.S., 2003, MNRAS, 340, 1375
- Pellegrini S., Fabbiano G., Fiore, F., Trinchieri G., Antonelli A. 2002, A&A, 383, 1
- Pellegrini S., Baldi A., Fabbiano G., Kim D.-W. 2003, ApJ, 597, 175
- Rasmussen J., Sommer-Larsen J., Pedersen K., Toft S., Benson A., Bower R.G., Grove L.F. 2009, ApJ, 697, 79
- Revnivtsev M., Churazov E., Sazonov S., Forman W., Jones C. 2007, A&A, 473, 783
- Revnivtsev M., Churazov E., Sazonov S., Forman W., Jones C. 2008, A&A, 490, 37
- Rubin V.C., Burstein D., Ford W.K. Jr., Thonnard N., 1985, ApJ, 289, 81
- Sansom A.E., O’Sullivan E., Forbes D.A., Proctor R.N., Davis D.S. 2006, MNRAS, 370, 1541
- Sarazin C.L., Irwin J.A., Bregman J.N. 2001, ApJ, 556, 533
- Sazonov S., et al. 2006, A&A, 450, 117
- Spitler L.R., Larsen S.S., Strader J., Brodie J.P., Forbes D.A., Beasley M.A. 2006, ApJ, 132, 1593
- Strickland D.K., Heckman T.M., Colbert E.J.M., Hoopes C.G., Weaver K.A. 2004, ApJS, 151, 193
- Strickland D.K., Heckman T.M., 2007, 658, 258
- Sutherland R.S., & Dopita M.A. 1993, ApJS, 88, 253
- Swartz D.A., Ghosh K.K., McCollough M.L., Pannuti T.G., Tennant A.F., Wu K. 2003, ApJS, 144, 213
- Tang S., Wang Q.D., Lu Y., Mo H.J. 2009a, MNRAS, 392, 77
- Tang S., Wang Q.D., Mac Low M.-M., Joung M.R. 2009b, MNRAS, 398, 1468
- Toft S., Rasmussen J., Sommer-Larsen J., Pedersen K., 2002, MNRAS, 335, 799
- Trinchieri G., Fabbiano G. 1985, ApJ, 296, 447
- Tullmann R., Pietsch W., Rossa J., Breitschwerdt D., Dettmar R.-J. 2006, A&A, 448, 43
- Tully, R. B. 1988, *Nearby Galaxies Catalog* (Cambridge: Cambridge University Press)
- Van Speybroeck L., Epstein A., Forman W., Giacconi R., Jones C., Liller W., Smarr L. 1979, ApJ, 234, L45
- Veilleux S., Cecil G., Bland-Hawthorn J. 2005, ARA&A, 43, 769
- Weisskopf M.C., Brinkman B., Canizares C., Garmire G., Murray S., Van Speybroeck L.P. 2002, PASP, 114, 1
- Wang Q.D. 2010, *Publications of the National Academy of Science*, Vol. 107, Iss. 16, p. 7168-7173
- White R.E.III, & Chevalier R.A., 1983, ApJ, 275, 69

White R.E.III, & Chevalier R.A., 1984, ApJ, 280, 561

White S.D.M., & Frenk C.S. 1991, ApJ, 379, 52

White S.D.M., & Rees M.J. 1978, MNRAS, 183, 341

Willingale R., Hands A.D.P., Warwick R.S., Snowden S.L., Burrows D.N., 2003, MNRAS, 343, 995

Yuan F., Yu Z., Ho L.C., 2009b, ApJ, 703, 1034

Zhang W.M., Soria R., Zhang S.N., Swartz D.A., Liu J.F. 2009, ApJ, 699, 281